Local Helioseismology: Three Dimensional Imaging of the Solar Interior

Laurent Gizon
Max-Planck-Institut für Sonnensystemforschung, Max-Planck-Straße 2, 37191 Katlenburg-Lindau, Germany; email: `gizon@mps.mpg.de`

Aaron C. Birch
NorthWest Research Associates, Colorado Research Associates Division, 3380 Mitchell Lane, Boulder, CO 80301, USA; email: `aaronb@cora.nwra.com`

Henk C. Spruit
Max-Planck-Institut für Astrophysik, Karl-Schwarzschild-Straße 1, 85748 Garching, Germany; email: `henk@mpa-garching.mpg.de`

Key Words Solar oscillations, convection zone dynamics, solar magnetism, sunspots, solar cycle

Abstract The Sun supports a rich spectrum of internal waves that are continuously excited by turbulent convection. The GONG network and the MDI/SOHO space instrument provide an exceptional data base of spatially-resolved observations of solar oscillations, covering an entire sunspot cycle (11 years). Local helioseismology is a set of tools for probing the solar interior in three dimensions using measurements of wave travel times and local mode frequencies. Local helioseismology has discovered (i) near-surface vector flows associated with convection (ii) 250 $\mathrm{m\,s^{-1}}$subsurface horizontal outflows around sunspots (iii) $\sim 50\ \mathrm{m\,s^{-1}}$extended horizontal flows around active regions (converging near the surface and diverging below), (iv) the effect of the Coriolis force on convective flows and active region flows (v) the subsurface signature of the 15 $\mathrm{m\,s^{-1}}$poleward meridional flow, (vi) a $\pm 5\ \mathrm{m\,s^{-1}}$time-varying depth-dependent component of the meridional circulation around the mean latitude of activity, and (vii) magnetic activity on the far side of the Sun.

CONTENTS

1 INTRODUCTION

Helioseismology is the observation and interpretation of the solar oscillations to probe the solar interior. These oscillations, with periods around five minutes, are due to the random superposition of acoustic waves and surface-gravity waves and are excited by turbulent convection in the upper layers of the Sun. Solar oscillations were discovered by Leighton, Noyes & Simon (1962) and interpreted by Ulrich (1970) and Leibacher & Stein (1971) as internal acoustic waves trapped in spherical-shell cavities. Wave motions are measured along the line of sight from the Doppler shifts of absorption lines in the solar spectrum. A short review of solar oscillations is given in Section 2.

Helioseismology has produced a large number of discoveries in solar, stellar, and fundamental physics. It provides the most precise tests of the theory of stellar structure and evolution, for example it motivated a revision of the standard model of particle physics to solve the solar neutrino problem. Helioseismology also enables the study and discovery of effects that are not included in standard solar models (standard models are spherically symmetric, non rotating, non magnetic, and include a simplified treatment of convection).

One of the most exciting aspects of helioseismology is the search for the origin of the Sun's magnetic field, one of the most important unsolved problems in solar physics. The eleven-year solar magnetic cycle is thought to be due to a field-amplification (dynamo-) process (cf. Charbonneau 2005, Rempel 2008), whereby a toroidal magnetic field component (in the azimuthal direction with respect to the rotation axis) is built up by stretching of the field lines by the Sun's differential rotation. In a second step the toroidal field is partially converted into a poloidal field component, which 'closes' the dynamo cycle. Models for this second step ('α-effect') differ significantly. In most models, it is attributed to the effect of convection on the magnetic field (convective dynamos). In an older model more closely connected with observations, convective flows play no role in this step; it is instead due to the instability of the toroidal field itself. The instability causes loops of magnetic field to rise to the solar surface, and appear as the observed magnetic (sunspot) activity. Resolution of this conflict between the models is key for progress towards a theory of stellar magnetic fields which has real predictive power. Helioseismology holds the promise of providing new observational constraints on cycle-related structures below the surface (e.g. Kosovichev 2008).

Traditionally, helioseismology methods have been classified into two groups: global helioseismology and local helioseismology. Global helioseismology consists of measuring the frequencies of the modes of oscillation and searching for seismic solar models whose oscillation frequencies match the observed ones (see Christensen-Dalsgaard 2002, for a review of techniques and results). Global helioseismology is two dimensional and is used to infer solar properties as functions of radius and unsigned latitude. A major achievement of global helioseismology is the inference of the angular velocity in the solar interior (e.g. Schou et al. 1998, Thompson et al. 2003). The differentially-rotating convection zone and the rigidly-rotating radiative interior are separated by a transition region at $0.69R_\odot$, the tachocline, which may be the seat of the solar dynamo.

Unlike standard global mode helioseismology, local helioseismology is capable of probing the solar interior in three dimensions. This is important for the study of solar activity, which is seen on the surface as localized patches of magnetic field, e.g. active regions, sunspots, and plage regions. Local helioseismology can potentially be used to infer vector flows, thermal and structural inhomogeneities, and even the magnetic field itself. Local helioseismology has been reviewed by e.g. Kosovichev & Duvall (1997), Braun & Lindsey (2000), Kosovichev, Duvall & Scherrer (2000), Christensen-Dalsgaard (2002), Kosovichev et al. (2002), Komm, Howe & Hill (2006), Gizon & Thompson (2007), Birch (2008), and Thompson & Zharkov (2008). The most comprehensive review is provided by Gizon & Birch (2005).

Local helioseismology encompasses various methods of data analysis (Section 3). One method of local helioseismology, ring diagram analysis, is a relatively straightforward extension of global helioseismology. It consists of measuring local frequencies of oscillation by analyzing small patches on the Sun. Ring-diagram analysis is computationally efficient and has produced important results, such as maps of flow patterns in the Sun.

Other methods of local helioseismology, like time-distance helioseismology and helioseismic holography, are based on the computation of the cross-covariance between the oscillation signal measured at two points on the surface. The basic principle is to retrieve information about the solar interior from the time it takes for solar waves to travel between any two surface locations through the solar interior. The cross-covariance function is directly related to the Green's function and thus carries essential information.

Like in global helioseismology, an inverse problem must be solved in order to retrieve subsurface solar properties from local helioseismic measurements (Section 4). In many cases it is acceptable to assume that the Sun is weakly heterogeneous in the horizontal directions: the inverse problem becomes a linear inverse problem and can be solved with standard techniques. However this is not always possible, especially in the presence of strong magnetic fields, e.g. in a sunspot.

Time-distance helioseismology aims at inferring subsurface properties at the best spatial and temporal resolution possible. A spatial resolution as small as a few Mm can be achieved near the surface. This limit is intimately linked to the smallest available horizontal wavelength of the solar oscillations (high frequency surface gravity waves). Detailed 3D maps of vector flows in the upper convection zone have provided new insights into the structure, evolution and organization of magnetic active regions and convective flows. The most easily detectable flow pattern is supergranulation, an intermediate-scale of convection (Section 5).

A particularly challenging aspect of local helioseismology is sunspot helioseismology (Section 6). Sunspots are regions of intense (kilogauss) magnetic field and low gas pressure and density. In spite of an abundance of telling clues from observations of the solar surface, theories about their formation, subsurface structure, thermal properties, and deep magnetic field topology are still controversial. The nature of solar waves is very significantly altered as they propagate through a sunspot and convert into magneto-acoustic-gravity (MAG) waves. Numerical modeling of wave propagation through model sunspots is currently being developed by several groups. These simulations will be key to interpret the solar oscillations in the vicinity of sunspots. Realistic numerical simulations also promise to be an important diagnostic tool for sunspot structure. The main question—what keeps a sunspot together as a clearly delineated entity?—may not ultimately be answerable by helioseismology, since key elements of the answer may well lie in a region near the base of the convection zone, where helioseismological tools may not have enough sensitivity to detect a sunspot-related signal. They may perhaps be sufficient, however, to challenge models that propose the origin of sunspots to be in the surface layers.

Among the most interesting results of local helioseismology is the detection of the subsurface meridional flow (Section 8). The meridional flow does not affect global mode frequencies (to first order) and thus has only been measured in the solar interior with local helioseismology. The meridional flow plays an important role in 'flux transport' theories, according to which the latitudinal transport of magnetic flux at the base of the convection zone determines the period of the solar cycle.

In yet another remarkable application, local helioseismology can be used to construct maps of active regions on the far side of the Sun (Section 9). In farside imaging, the Sun as whole is used as an acoustic lens focussing waves at a point on the invisible hemisphere. Maps of the farside are potentially important to predict space weather and provide advance warning for coronal mass ejections and solar flares (violent and sudden release of energy associated with the reconfiguration of the magnetic field in the atmosphere above an active region). Flares can excite acoustic waves to measurable levels, which can in turn tell us about the physics of flares (Section 10).

These examples illustrate the many facets of the science possible with local helioseismology, as summarized in **Figure 1**. In all these cases a taste of the possibilities has been provided, but improved observations (Section 11) and further developments in the techniques of analysis and interpretation are required to realize the full potential of local helioseismology.

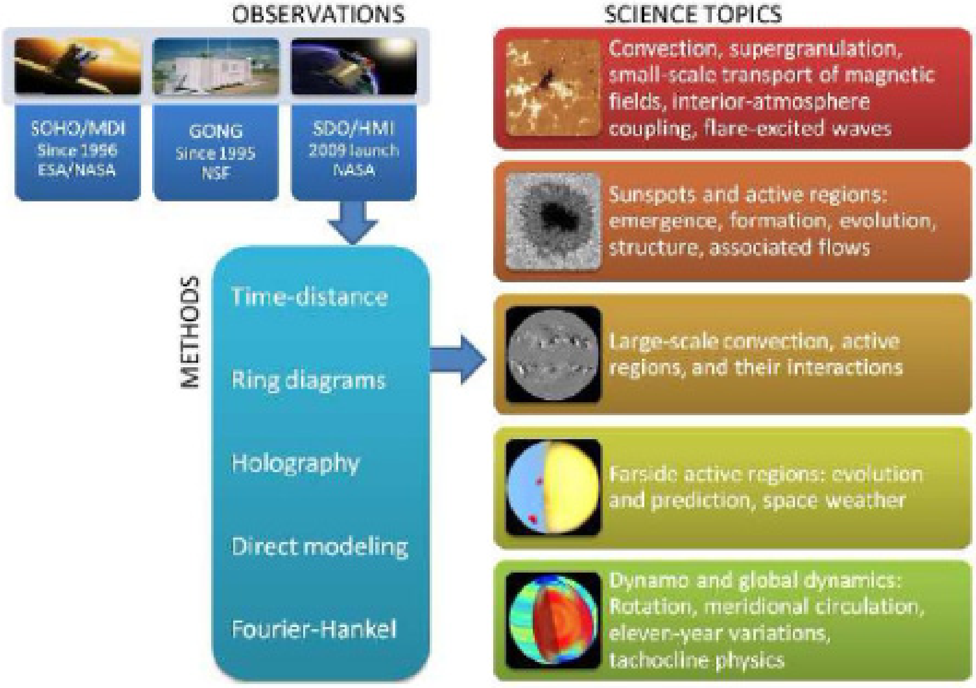

Figure 1: Overview of local helioseismology: Observational data, methods of analysis, and scientific applications.

2 SOLAR OSCILLATIONS

2.1 Observations

In most cases, local helioseismology uses time-series of Dopplergrams as input data. A Dopplergram is a digitized image of the line-of-sight velocity of the solar surface (photosphere or chromosphere) deduced from the Doppler shifts of a Fraunhofer absorption line (e.g., Scherrer et al. 1995). Solar oscillations have a higher signal-to-noise ratio in Doppler velocity than in intensity, especially at low frequencies.

There are two major data sets available for local helioseismology. The first one is provided by the Global Oscillation Network Group (GONG, Harvey et al. 1996) headquartered in Tucson, Arizona, which operates a global network of six stations around the world. The sites are distributed in longitude in order to observe continuously: Big Bear (California), Mauna Loa (Hawaii), Learmonth (Australia), Udaipur (India), El Teide (Canary Islands), and Cerro Tololo (Chile). The cadence of the observations is one minute to avoid temporal aliasing. Each GONG instrument is a phase-shift interferometer that measures the phase of the Fourier transform of the solar spectrum around the Ni I absorption line at 6768 Å, interpreted as a Doppler shift (Harvey & The GONG Instrument Team 1995). While the original cameras had an image size of 256×256 pixels, full-disk Dopplergrams have been recorded with 1024×1024 CDD cameras since 2001, hence providing a good spatial resolution (5 arcsec) for local helioseismology. The GONG instruments also acquire intensity images and line-of-sight magnetograms. The effective duty cycle of the merged observations is over 90%.

The other main data set is provided by the Michelson Doppler Imager (MDI, Scherrer et al. 1995) on-board the ESA/NASA Solar and Heliospheric Observatory (SOHO), which was launched in December 1995. SOHO is in a halo orbit around the Sun-Earth L1 Lagrange point. Observations from SOHO are not only continuous, but benefit from perfect seeing and from a slowly varying spacecraft-to-Sun velocity. The MDI filter system relies on two tunable Michelson interferometers in order to measure intensity in five very narrow filters (94 mÅ) in the wings and core of the Ni 6768 line. The Doppler velocity is obtained by taking the difference between filtergrams on each side of the absorption line. The MDI observables are the line depth and continuum, line-of-sight Doppler velocity, and line-of-sight magnetic field. The temporal cadence is one minute and the CCD camera has 1024×1024 pixels. It can operate in two different modes: a full-disk mode (2 arcsec pixel) or a high-resolution mode (0.6 arcsec pixel). **Figure 2** shows example full-disk SOHO/MDI observables and **Supplemental Movie 1** shows a time series of full-disk Dopplergrams. In high-resolution mode, the resolution is better by a factor of three but the field of view is reduced. Because of limited telemetry, the full-disk Dopplergrams have only been transmitted at full cadence for about two to three months each year since 1996, while the high-resolution Dopplergrams are reserved for targeted campaigns of observation. The rest of the time, the Dopplergrams are spatially filtered onboard and converted into lower-resolution 256×256 images, in order to save telemetry ('medium-degree' data).

GONG and MDI are complemented by other data sets, e.g. from the Taiwan Oscillation Network (TON, Chou et al. 1995), from campaigns of observations at the South Pole with the Magneto-Optical filter at Two Heights (MOTH, Finsterle et al. 2004a), and from the Hinode satellite (e.g. Mitra-Kraev, Kosovichev & Sekii 2008).

In many applications of local helioseismology, the standard procedure consists of choosing a relatively small region of the Sun and following (or 'tracking') it in a frame that is co-rotating with the Sun. This gives a time series of Doppler images that are centered on the region of interest, like a magnetic active region. In this process each individual image is mapped onto a common spatial grid.

For local studies it is often convenient to neglect the curvature of the solar surface and work in plane-parallel geometry. With this simplification, it is natural to study the oscillations in three-dimensional Fourier space. The oscillation signal, denoted by $\phi(\mathbf{r}, t)$, where $\mathbf{r} = (x, y)$ is the horizontal position vector and

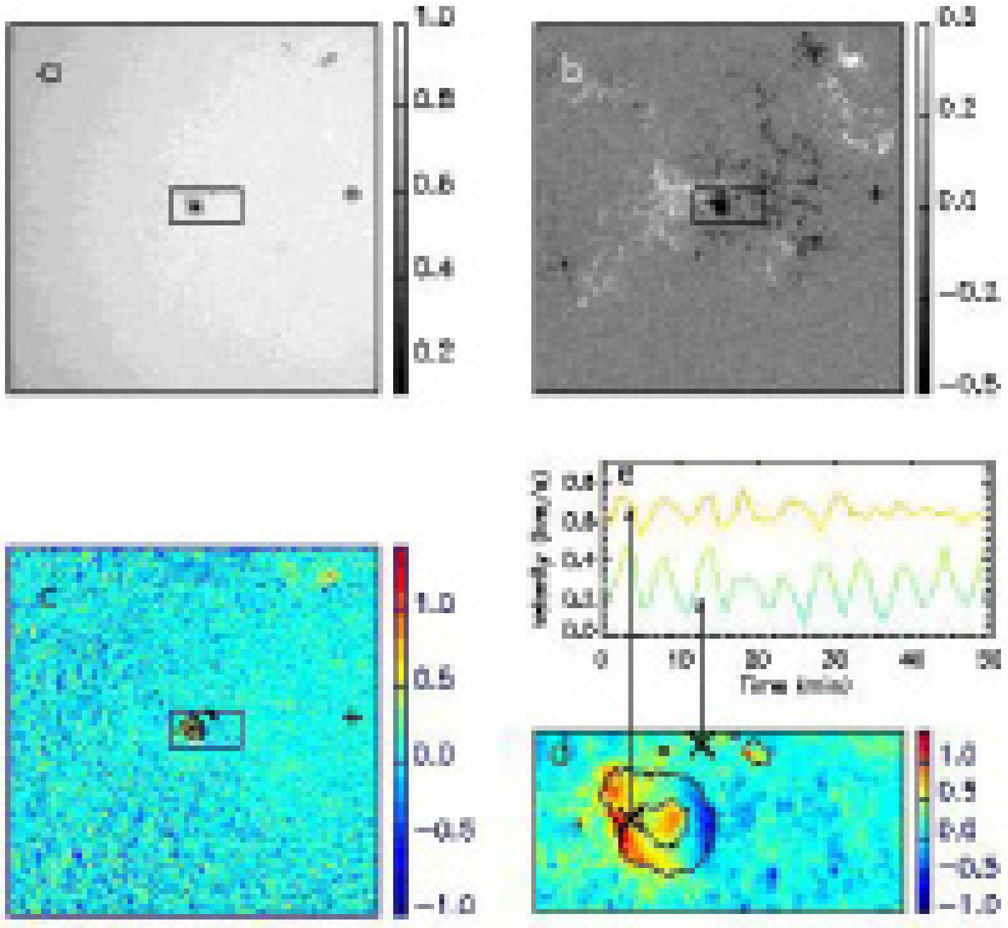

Figure 2: SOHO/MDI observations on 22 January 2008 at 17:36:00 remapped using Postel's azimuthal equidistant projection with a map scale of 0.12 deg/pixel or 1.46 Mm/pixel. The sunspot in Active Region NOAA 9787 is at the center of projection. (*a*) 512×512 pixel subfield of the continuum intensity, normalized to unity at disk center (plus sign). The box around the sunspot has size 147 Mm × 73 Mm. (*b*) Line-of-sight component of the magnetic field in kG (truncated gray scale). (*c*) Line-of-sight Doppler velocity in $\mathrm{km\,s^{-1}}$. Supergranulation is visible toward the edges of the frame. (*d*) Doppler velocity in the sunspot box. The black contours give the outer edges of the umbra and penumbra of the sunspot. The center-to-disk component of the Evershed outflow is visible in the penumbra. (*e*) Doppler velocity as a function of time at the two locations denoted by the crosses in panel *d*. The five minute period of the solar oscillations is evident. The oscillations have reduced amplitudes in the sunspot.

t is time, is decomposed into harmonic components

$$\phi(\mathbf{k},\omega) = \int_A \mathrm{d}^2\mathbf{r} \int_0^T \mathrm{d}t \; \phi(\mathbf{r},t)\; e^{-i\mathbf{k}\cdot\mathbf{r}+i\omega t}, \tag{1}$$

where A is the area of study, T is the total observation time, the vector $\mathbf{k} = (k_x, k_y)$ is the horizontal wavevector, and ω is the angular frequency. The horizontal wavenumber is $k = \|\mathbf{k}\|$. By convention, the x coordinate is positive in the direction of rotation (prograde) and the y coordinate points north. The power spectrum of solar oscillations is defined as

$$P(\mathbf{k}, \omega) = |\phi(\mathbf{k}, \omega)|^2. \tag{2}$$

We note that the spatial Fourier transform should be replaced by a spherical harmonic transform when curvature effects cannot be ignored, as in global helioseismology.

An example power spectrum of solar oscillations is shown in **Figure 3**. Power is distributed along well-defined discrete ridges in wavenumber-frequency space and peaks around 3 mHz. The first ridge at low frequencies shows the “fundamental” (f) modes. These are surface gravity waves with exponential eigenfunctions and a dispersion relation $\omega^2 = gk$, where $g = 274\ \mathrm{m\,s^{-2}}$is the acceleration of gravity at the solar surface; they are similar to waves at the surface of a deep ocean. All other ridges correspond to pressure (p) modes, i.e. acoustic waves modified by gravity. The existence of discrete ridges, $\omega = \omega_n(k)$ with $n > 0$, reflects the fact that p modes are trapped in the vertical direction. At fixed wavenumber, the peaks of power are labeled p_0, p_1, p_2, etc. with increasing frequency. A mode p_n is such that the number of radial nodes of the mode displacement is n (the radial order). By convention, the f modes are labeled with $n = 0$. All ridges have reduced power above 5.3 mHz, which is the cut-off frequency above which waves are not reflected back into the Sun but escape into the atmosphere. The frequency width of a ridge is inversely proportional to the mode lifetime. A recent description of the mode parameters, including mode lifetimes, is provided by Korzennik, Rabello-Soares & Schou (2004).

2.2 Modes

In order to better understand the diagnostic capability of each mode, it is useful to consider simple solar models. For our purpose, a simple solar model is a reference standard solar model, which only depends on height (or radius), such as Model S (Christensen-Dalsgaard et al. 1996). In plane-parallel models that are isotropic and translation invariant in the horizontal directions, the normal modes of the oscillations of the model vary horizontally as $\exp(i\mathbf{k}\cdot\mathbf{r})$. For the case of p and f modes, it is convenient to introduce the mode eigenfunctions $U_n(z;k)$ and $V_n(z;k)$ such that the complex displacement eigenfunction of the mode characterized by radial order n and horizontal wavevector $\mathbf{k}$ is

$$\boldsymbol{\xi}_n(\mathbf{r}, z; \mathbf{k}) = \left[\hat{\mathbf{z}} U_n(z;k) + i\hat{\mathbf{k}} V_n(z;k)\right] e^{i\mathbf{k}\cdot\mathbf{r}}, \tag{3}$$

where z is height, $\hat{\mathbf{z}}$ is the unit vector pointing upwards, and $\hat{\mathbf{k}}$ is the horizontal unit vector pointing in the direction of $\mathbf{k}$. Zero height corresponds to the photo-

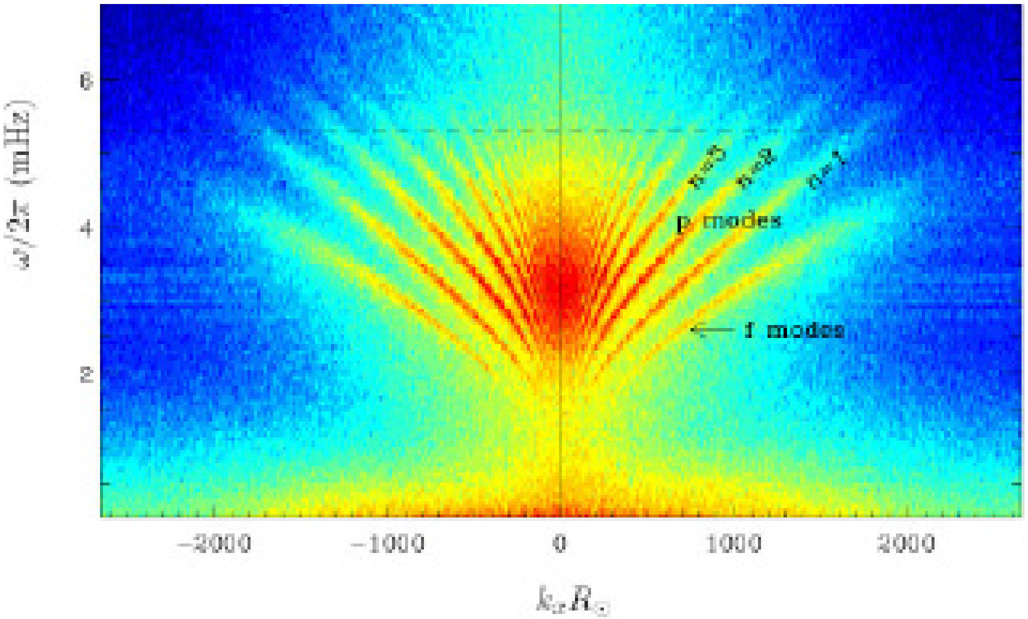

Figure 3: Cut at $k_y = 0$ through an average power spectrum of MDI/SOHO high-resolution Doppler velocity data as a function of frequency and $k_x R_\odot$. The horizontal dashed line shows the acoustic cutoff frequency. In order to reduce random noise, an average was carried out over eight individual power spectra, each of duration $T = 4$ hr and covering an apodized region of area $A \sim (500\ \mathrm{Mm})^2$. Since $k_y = 0$, only waves traveling in the east or west directions are showed. The power below ~ 1.5 mHz is due to solar convection, granulation and supergranulation.

sphere ($-z$ is depth). The representation of the displacement eigenfunctions in terms of only the two functions U and V is possible as neither the f nor the p modes have horizontal motions that are perpendicular to $\mathbf{k}$. As a result of the assumed isotropy, the functions U and V do not depend on the direction of $\mathbf{k}$ and the mode frequencies $\omega_n(k)$ only depend on wavenumber. The time evolution of the mode $(n, \mathbf{k})$ is given by $\exp[-i\omega_n(k)t]$. In models that include attenuation, the frequencies are complex, while they are real for the case of adiabatic oscillations and standard boundary conditions.

Figure 4 shows the horizontal and vertical eigenfunctions corresponding to the first five radial orders at a frequency of 3.5 mHz. The solar model for this case is a plane-parallel version of Model S. The eigenfunctions are scaled by $\rho^{1/2}$, where ρ is the density (left-most panel). This scaling is used as we are interested in the kinetic energy density of the modes, $\rho(U^2 + V^2)$, which is a physically relevant quantity. For the f mode the horizontal and vertical displacement eigenfunctions are equal. For the acoustic modes ($n > 0$), the lower turning point, z_t, is the height at which the sound speed is equal to the horizontal phase speed of the mode: $c(z_\mathrm{t}) = \omega/k$ (neglecting the buoyancy frequency and the acoustic cutoff frequency, both of which are very small below a few Mm beneath the photosphere). Thus all the modes with a similar horizontal phase speed (a straight

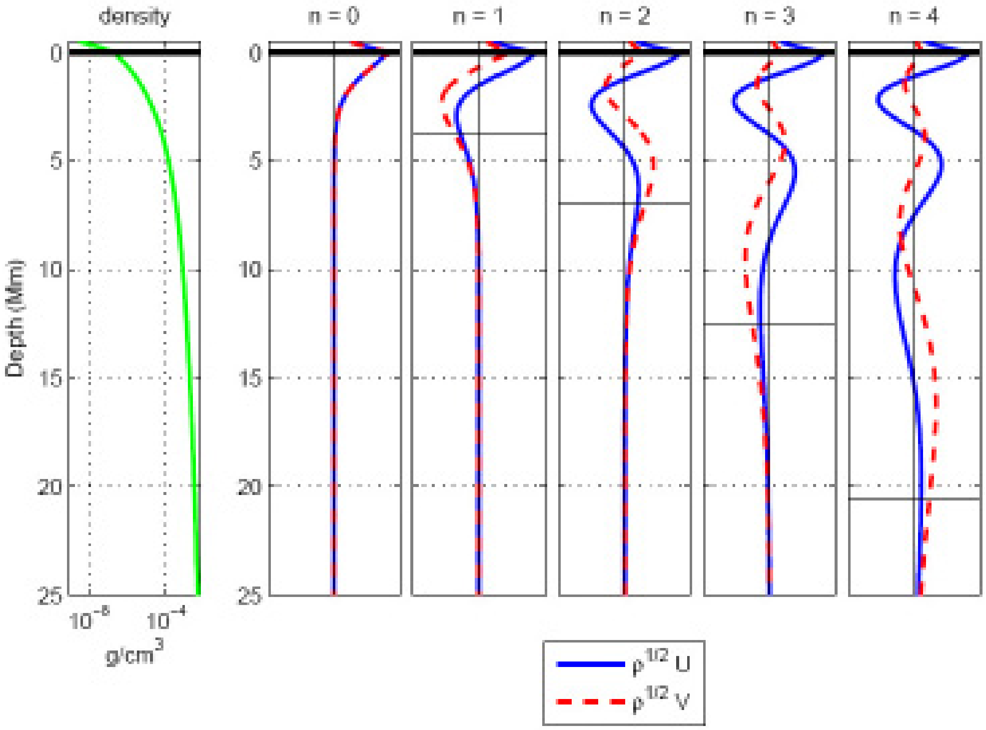

Figure 4: Density profile from Model S (left panel, green line) and mode eigenfunctions U and V for the radials order $n = 0-4$ (other panels) at the frequency 3.5 mHz. The lower turning points of the modes $n = 1-4$ are shown as thin horizontal black lines. At fixed frequency, the horizontal phase speed ω/k increases with increasing radial order n, and therefore lower turning points increase with increasing n as well. The functions U and V have been scaled with $\rho^{1/2}$ as the kinetic energy density is proportional to $\rho(U^2 + V^2)$.

line through the origin in **Figure 3**) have a similar lower turning point and probe essentially the same layers of the Sun.

3 LOCAL HELIOSEISMOLOGY

In this section we give an overview of the various methods of local helioseismology. For an in-depth description of each method see e.g. Gizon & Birch (2005) and references therein.

3.1 Ring Diagram Analysis

The first operation in ring diagram analysis is to cover some fraction of the visible solar disk with patches (overlapping or not) with circular areas with diameters in the range $2^\circ - 30^\circ$. Each patch is tracked in longitude with a velocity close to the solar surface rotation velocity to produce a time series of helioseismic observations (Dopplergrams or intensity images). For each patch a three-dimensional local power spectrum of the solar oscillation, P, is computed according to Equations 1 and 2. The local power spectra reflect the local physical conditions in the solar interior, such as wave speed and horizontal flows (Hill 1988). For example, a constant horizontal flow $\mathbf{u}$ will introduce a Doppler shift of the power spectrum:

$$P(\mathbf{k}, \omega) = P_0(\mathbf{k}, \omega - \mathbf{k} \cdot \mathbf{u}), \tag{4}$$

where P_0 is the power spectrum in the absence of a flow. This description is highly simplified as flows in the Sun do vary with horizontal position and depth. A change in the structure of the solar interior produces a change in the dispersion relation that does not depend on the direction of $\mathbf{k}$, and thus a change in the power spectrum that is also independent of the direction of $\mathbf{k}$.

There are two ways to study local power spectra. The first approach is to consider cuts at constant frequency, ω. In (k_x, k_y) space, wave power is concentrated in rings, each corresponding to a different radial order n (Hill 1988). A ring diagram is shown in **Figure 5**. When there is no flow, the radius of each ring is the wavenumber k at which $\omega_n(k) = \omega$ and is sensitive to the local dispersion relation. Thus the ring radius is related to the local wave speed under the patch. As shown above, a flow will affect the local power spectrum. Linearizing Equation 4 for small $\mathbf{k} \cdot \mathbf{u}$, we find that the change in the ring position is $\delta\mathbf{k} = -(k/v_\mathrm{g})\mathbf{u}$, where $v_\mathrm{g} = \partial_k \omega_n$ is the group speed. Hence the flow amplitude and direction can be estimated from the distortion and orientation of the distorted rings. Note that the distortion of a ring depends on radial order in the case of a depth-varying flow.

The second approach consists of considering cuts at constant wavenumber, k, through the power spectra (Schou & Bogart 1998). The local power spectra are then studied in (ψ, ω) space, where ψ is the azimuth of the wave vector measured from the prograde direction, $\hat{\mathbf{x}}$. The modes appear as bands of power around the resonant frequencies $\omega_n(k)$. According to Equation 4, a constant horizontal flow will Doppler shift the mode frequencies by $\delta\omega = \mathbf{k} \cdot \mathbf{u} = k u_x \cos\psi + k u_y \sin\psi$. As a result, $\mathbf{u}$ can be estimated from the frequency shifts at each k and radial order n. A change in the wave speed will simply manifest itself as a change in the wave frequencies that is independent of ψ and can be disentangled from the effect of a horizontal flow.

Both approaches rely on fitting a parametric model of the power spectrum to the observed local power spectra. Several functional forms have been proposed to fit the observations. The most important fitted parameters are the mode frequencies, $\overline{\varpi}(n, k)$, and the two flow parameters, $\overline{u}_x(n, k)$ and $\overline{u}_y(n, k)$. There is one set of parameters for each wavenumber and radial order. Details about the fitting procedures are given by, e.g., Basu, Antia & Tripathy (1999) for the first approach and, e.g., Haber et al. (2000) for the second approach.

The fitted parameters are sensitive to the conditions in the solar interior, with a

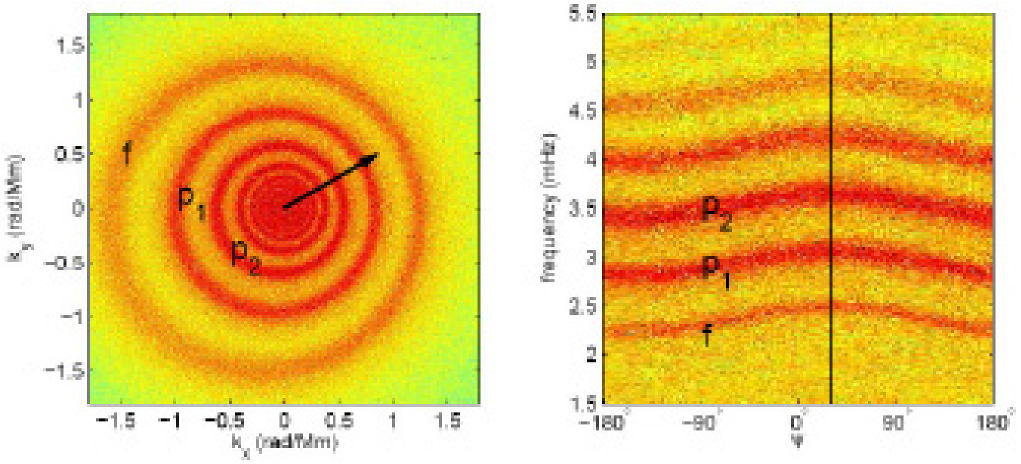

Figure 5: Slices through a model local power spectrum at constant frequency $\omega/2\pi = 3.1$ mHz (*left*, ring diagram) and at constant wavenumber $k = 0.8$ rad/Mm (*right*) for the case of a depth-independent horizontal flow $\mathbf{u}$ with an amplitude of 1 km/s and in the direction ψ_0 that is thirty degrees north of the prograde direction. In the left panel, the black arrow shows the direction of the flow. The different rings correspond to different radial orders; the outermost ring is the f mode. The rings with large k are more strongly influenced by the flow than those with small k (see text). In the right panel, the ridge frequencies show a sinusoidal variation with ψ and reach their maxima when $\psi = \psi_0$ (shown by the vertical black line). The frequency variation with ψ is the same for all of the ridges as as the flow is independent of depth.

depth sensitivity that depends on the eigenfunction of the mode (e.g. Christensen-Dalsgaard 2002). For example, the depth sensitivity to a horizontal flow is approximately given by the kinetic energy density of the mode (e.g. Birch et al. 2007). The larger the horizontal phase speed of the mode, the deeper the sensitivity. Thus large patches give access to deeper regions in the Sun than small patches. The differences between the fitted mode frequencies, $\overline{\omega}$, and the mode frequencies calculated from a standard solar model, $\omega_n(k)$, are used in one dimensional (depth) inversions to infer structural conditions under each patch (e.g. Basu, Antia & Bogart 2004). Two independent structural quantities can be inverted at a time, e.g., sound speed and density, from which other quantities can be inferred, such as the first adiabatic exponent. Similarly, the depth dependence of the horizontal flows, u_x and u_y, can be inferred from a set of fitted parameters $\overline{u}_x$ and $\overline{u}_y$ (Hill 1989). Typically, ring analysis is used to probe the top 30 Mm of the convection zone, with a maximum horizontal resolution of about 2° near the surface. Three-dimensional maps can then be obtained by combining neighboring patches.

3.2 The Cross-Covariance Function

Time-distance helioseismology is based on the measurement of the cross-covariance between the Doppler signals at two points $\mathbf{r}_1$ and $\mathbf{r}_2$ on the solar surface,

$$C(\mathbf{r}_1, \mathbf{r}_2, t) = \int_0^T \mathrm{d}t' \; \phi(\mathbf{r}_1, t')\phi(\mathbf{r}_2, t' + t) \; , \tag{5}$$

where t is the correlation time-lag. **Figure 6*a*** shows a cross-covariance function measured from 144 days of MDI medium-degree data. The cross-covariance has been averaged over many pairs of points $(\mathbf{r}_2, \mathbf{r}_1)$ and is presented as a function of the heliocentric angle between these two points. This diagram is known as the "time-distance diagram." The cross-covariance is essentially a phase coherent average of the random oscillations (Bogdan 1997, and **Supplemental Movie 2**). It is a solar seismogram: it provides a way to measure wave travel times between two surface locations.

A particular wave packet (consisting of set of modes with similar phase speeds) is preferentially selected for each travel distance. Many applications involve much less temporal and spatial averaging than was used in this figure. Typical cross-covariances are therefore much noisier than the example shown here. The deeper meaning of the cross-covariance was elucidated only recently in terms of Green's functions (see **Side Bar**).

An important tool for visualizing wave propagation in the Sun is the ray approximation (e.g. Kosovichev & Duvall 1997). In this approximation, the wavelength is treated as if it were much smaller than the length scales associated with the variations in the background solar model. The ray paths describe the propagation of wave energy and are analogous to the rays in geometrical optics. For discussions of the range of validity of the ray approximation see e.g. Hung, Dahlen & Nolet (2000) and Birch et al. (2001).

Figure 6*b* shows some example ray paths computed from Model S. In this figure, the rays all begin from the same point at the solar surface. Downward propagating rays are refracted by the increase of the sound speed with depth until they reach their lower turning where the horizontal phase speed matches the sound speed. At frequencies below about 5.3 mHz, upwards propagating rays are reflected from the solar surface by the sharp rise in the acoustic cutoff frequency. At higher frequencies, the waves escape into the solar atmosphere.

The main features in the time-distance diagram (**Figure 6*a***) are the ridges which correspond to different paths that wave energy takes between pairs of observation points. For example, the blue line corresponds to "first-bounce" arrivals (i.e., waves that visit their lower turning points once between the two observation points). The fine structure of the ridges in the time-difference diagram reflects the band-limited nature of the power spectrum. The majority of the wave power is near 3 mHz and as a result the cross-covariance shows fine structure that has a period of about 5 min. The other ridges seen in the time-distance diagram correspond to multiple bounces. One particularly important ray path is the third bounce ray path (green $3'$) that travels to the farside of the Sun before returning to the visible disk, this ray path plays a central role in farside imaging (Section 9). As can be seen in the example ray paths in **Figure 6*b***, the depth of the lower turning point increases with the distance the ray travels in a single skip.

We note that the cross-covariance is directly related to the local power spectrum in the case when the medium is assumed to be horizontally invariant over this local area. In this case, the cross-covariance is simply given by the inverse Fourier transform of the local power spectrum (Gizon & Birch 2002):

$$C(\mathbf{r}_1, \mathbf{r}_2, t) = \text{const.} \int \mathrm{d}^2\mathbf{k} \int \mathrm{d}\omega \; P(\mathbf{k}, \omega) e^{i\mathbf{k}\cdot(\mathbf{r}_2 - \mathbf{r}_1) - i\omega t}. \tag{6}$$

Changes in the local power spectrum, such as those discussed above in the context of ring-diagram analysis, will affect the cross-covariance.

3.3 Time-Distance Helioseismology

Time-distance helioseismology (Duvall et al. 1993, 1997, Kosovichev 1996) consists of (i) measuring wave travel times from the cross-covariance function, and (ii) inverting the travel times to infer the solar subsurface structure and flows.

As discussed in the **Side Bar**, the cross-covariance $C(\mathbf{r}_1, \mathbf{r}_2, t)$ is closely related to a Green's function that gives the wave response at $(\mathbf{r}_2, t)$ to a source located at $(\mathbf{r}_1, t = 0)$. Thus the cross-covariance is sensitive to the wave propagation conditions (structure and flows) between the two surface points $\mathbf{r}_1$ and $\mathbf{r}_2$. The sensitivity of the cross-covariance to any particular local change in the solar interior is a non-trivial research topic, because the local wavelength of solar oscillations is not necessarily small compared to the length scales of the heterogenities in the Sun. In addition, this sensitivity depends strongly on the combination of waves that contribute to the cross-covariance function. This will be discussed in Section 4.

For the sake of simplicity, consider a constant horizontal flow $\mathbf{u}$. According to Equations 6 and 4, the effect of such a flow is a Galilean translation of the unperturbed (no flow) cross-covariance, C_0, according to:

$$C(\mathbf{r}_1, \mathbf{r}_2, t) = C_0(\mathbf{r}_1, \mathbf{r}_2 - \mathbf{u}t, t). \tag{7}$$

In practise, this result is only an approximation because the power spectrum is often subject to additional filtering, which is not included in Equation 6 (Gizon & Birch 2002). The waves travel faster along the flow than against the flow. If $\mathbf{u}$ is directed from $\mathbf{r}_1$ to $\mathbf{r}_2$, then the $t > 0$ ridges of the time-distance diagram will be shifted to smaller time-lags t and the $t < 0$ ridges will be shifted to more negative t. Thus a flow will break the symmetry between the $t > 0$ and $t < 0$

parts of the cross-covariance. In contrast, a horizontally uniform change in, e.g., sound speed would introduce a time-symmetric change in the cross-covariance.

Several techniques have been proposed to measure travel times from the cross-covariance. The (phase) travel times for inward- and outward-going waves are measured by fitting a Gabor wavelet to the two branches of the cross-covariance (Duvall et al. 1997, Kosovichev & Duvall 1997). The travel times can also be measured with a simple one-parameter fit (Gizon & Birch 2002, 2004), as is done in geophysics (e.g. Marquering, Dahlen & Nolet 1999).

The cross-covariance function computed between two spatial points is in general very noisy. Spatial averaging is a useful tool to reducing random noise. Duvall et al. (1997) considered an averaging scheme whereby the cross-covariance is computed between a point and a concentric annulus or quadrants of arc. For example, the cross-covariance between a point and an annulus is used to study waves that propagate outward from the central point to the annulus (positive time-lag) and inward (negative time-lag). The difference between inward and outward travel times is sensitive to the horizontal divergence of the local flow or to a local vertical flow, while the average travel time is sensitive to the local wave speed. Similarly, the covariance between a point and a north quadrant is used to study waves that propagate either northward or southward. The various combinations of travel times are shown in **Figure 7** for annulus radii ranging from 12 Mm to 27 Mm. Each travel-time map is obtained by translating the central point of the annulus. With only a few hours of averaging, it is clear that the travel-times differences are sensitive to the supergranulation flows.

Finally, the travel-time maps must be inverted (the inverse problem). This requires a model for the relationship between the travel-time perturbations and perturbations in solar properties (the forward problem). Recent progress regarding the interpretation of traveltimes is described in Section 4.

3.4 Helioseismic Holography

Helioseismic holography (Lindsey & Braun 1997) and acoustic imaging (Chang et al. 1997), which are virtually indistinguishable, are closely related to the time-distance method. In both of these methods, observations of the wavefield (e.g. Doppler velocity) at the solar surface are used to estimate the wavefield in the solar interior. Separate estimates are constructed by computationally evolving the observed wavefield either forwards or backwards in time. In helioseismic holography, these two estimates are called the ingression (H_-, propagates forwards in time) and egression (H_+, propagates backwards in time) and are computed as

$$H_\pm(\mathbf{r}, z, \omega) = \int_{\mathcal{P}} \mathrm{d}^2\mathbf{r}'\, G_\pm(\|\mathbf{r}' - \mathbf{r}\|, z, \omega)\phi(\mathbf{r}', \omega), \tag{8}$$

where $\mathbf{r}$ is the horizontal focus position, z is the focus depth, and the integration over surface positions $\mathbf{r}'$ is carried out over the region described by the "pupil" $\mathcal{P}$. The functions $G_\pm$ are causal (subscript $-$) and anti-causal (subscript $+$) Green's functions. These Green's functions can be thought of as propagators which (approximately) evolve the wavefield either forwards or backwards in time.

The amplitude and phase of the correlation between the two estimates $H_\pm$ contain information regarding wave propagation in the Sun (e.g. Lindsey & Braun 1997, 2000). For example, in farside imaging (Section 9), the phase of the ingression-egression correlation is used to detect active regions.

3.5 Direct Modeling

Direct modeling (Woodard 2002, 2007) is a method for interpreting correlations in the wavefield. These correlations, however, are not measured in real space but in the Fourier domain. For example, any steady heterogeneity in the Sun is expected to introduce correlations between incoming and scattered waves with different wave vectors but the same frequency. Unlike time-distance helioseismology, direct modeling can also treat time-varying perturbations, which couple waves with different frequencies. One of the main characteristics of direct modeling, as its name suggests, is that it does not produce any intermediate data products (e.g. no travel time map) as the inversions are carried out directly on the correlations.

3.6 Fourier-Hankel Analysis

Fourier-Hankel analysis (Braun, Duvall & Labonte 1987) was specifically designed to study the wavefield around sunspots. The analysis is carried out in a cylindrical coordinate system with origin centered on the sunspot. The wavefield observed in an annular region around the sunspot is decomposed into inward and outward propagating components, using a Fourier-Hankel transform. The amplitudes and the phases of the incoming and outgoing waves can be compared in order to characterize the interaction of the waves with the sunspot. In particular Fourier-Hankel analysis was the first method to measure the absorption coefficient of incoming waves by a sunspot (Braun, Duvall & Labonte 1987), defined by $(P_{\rm in} - P_{\rm out})/P_{\rm in}$, where $P_{\rm in}$ and $P_{\rm out}$ are respectively the incoming and outgoing powers. In addition, the Fourier-Hankel method has been used to measure the phase shift between the incoming and outgoing waves, as well as the scattering from one mode to another (Braun 1995).

4 THE FORWARD AND INVERSE PROBLEMS

4.1 Weak Perturbation Approximation

Many important solar features can be reasonably approximated, in the context of wave propagation, as small deviations from a horizontally uniform reference model. Examples include the supergranulation, meridional flow, torsional oscillations, and subsurface (but not surface) magnetic fields. For this class of solar features, linear forward modeling can be employed. The main advantage of linear forward models is that they lead to linear inverse problems, which is the only class of inverse problems that can be solved easily.

4.1.1 **Sensitivity functions.** In linear forward models, the helioseismic measurements (e.g., travel-time shifts) can be related to weak, steady, perturbations to a reference model through sensitivity functions (also called kernels) by equations of the form

$$d_i = \sum_\alpha \int_\odot K_i^\alpha(\mathbf{x}) \delta q_\alpha(\mathbf{x}) \mathrm{d}^3\mathbf{x} \ , \tag{9}$$

where the d_i stand for an arbitrary set of helioseismic measurements (for example travel-time perturbations $\delta\tau_i$), the functions δq_α describe the deviations from the reference solar model, and the functions K_i^α are the corresponding kernel functions. The sum over α is over all types of perturbations to the solar model. A complete set of q_α includes, e.g., pressure, density, sound speed (c), flow velocity ($\mathbf{u}$), and magnetic field vector ($\mathbf{B}$). The integration variable $\mathbf{x}$ is a three-dimensional position vector and runs over the entire reference solar model.

4.1.2 **The ray approximation.** The ray approximation, in which the wavelength is approximated as small compared to the other length scales in the problem (e.g., the scale heights of the reference model, and the length scales of the perturbations δq^α) has been used extensively in time-distance helioseismology (e.g. Kosovichev 1996, Kosovichev & Duvall 1997) to compute the travel-time sensitivity functions K. A ray sensitivity kernel for the travel-time perturbation $\delta\tau(\mathbf{r}_1, \mathbf{r}_2)$, is zero everywhere except along the ray, Γ, that goes from $\mathbf{r}_1$ to $\mathbf{r}_2$ (see Section3.2).

The starting point is the local dispersion relation:

$$(\omega - \mathbf{k}_\mathrm{t} \cdot \mathbf{u})^2 = c^2 k_\mathrm{t}^2 + \omega_\mathrm{ac}^2, \tag{10}$$

where ω is the angular frequency, $\mathbf{k}_\mathrm{t}$ is the three-dimensional total wave vector, $\mathbf{u}$ is the vector flow, c is the sound speed, and ω_ac is the acoustic cut-off frequency. In the ray approximation the travel time is given by the path integral of the phase slowness vector $\mathbf{k}_\mathrm{t}/\omega$. Under the assumption that ω is constant, the travel time perturbation is given by

$$\delta\tau = \frac{1}{\omega}\int_{\Gamma} \delta\mathbf{k}_{\rm t}\cdot\hat{\mathbf{n}}\,{\rm d}s, \qquad (11)$$

where $\hat{\mathbf{n}}$ is the unit vector along Γ and $\delta\mathbf{k}_{\rm t}$ is the perturbation to the total wave vector caused by the flow $\mathbf{u}$, the change in the sound speed, δc, and the change in the acoustic cut-off frequency, $\delta\omega_{\rm ac}$. Notice that the ray path, Γ, is assumed to be unchanged to first order. Although the ray approximation has played an important role in local helioseismology, it does not account for finite wavelength effects and other complications (cf. Birch et al. 2009, Bogdan 1997).

4.1.3 **The first Born approximation.**

In the first-order Born approximation, the perturbations δq_α cause a perturbation to the wave field that is due to single scattering only. In this approximation, first-order finite wavelength effects, such as Fresnel zones and wavefront healing, are included (e.g., Hung, Dahlen & Nolet 2001). The Born approximation has been used in the seismology of the Earth (e.g., in the search for mantle plumes by Montelli et al. 2004). Gizon & Birch (2002) give a detailed theoretical treatment of the application of the Born approximation to problems in time-distance helioseismology.

Born kernels for the effects of sound-speed changes on travel times have been obtained by, e.g., Birch & Kosovichev (2000) and Jensen, Jacobsen & Christensen-Dalsgaard (2000). Born kernels for flows have been computed for time-distance helioseismology by Gizon, Duvall & Larsen (2000), Birch et al. (2007), and Jackiewicz et al. (2007). Three-dimensional sensitivity kernels for flows and ring-diagram analysis are given by Birch & Gizon (2007). Although magnetic perturbations are expected to be small just a few hundred km below the surface (Gizon, Hanasoge & Birch 2006), corresponding kernels have not been obtained yet.

Figure 8 shows slices through an example travel-time sensitivity kernel for perturbations in the squared sound-speed ($\delta d_i = \delta\tau$ and $q_\alpha = c^2$ in Equation 9). The main features are that the kernel is zero along the ray path, is maximum (absolute value) in a shell around the ray path, and shows substantial ringing. These kernels have been called “banana-doughnut kernels” in the context of seismology of the Earth (Marquering, Dahlen & Nolet 1999).The zero along the ray path is due to the lack of a geometrical delay (change in path length) for small scatterers located on the reference ray path. In the solar case, there are additional hyperbolic features across the ray path, due to the presence of distant sources (Gizon & Birch 2002).

The first-order Born approximation have been tested using exact solutions (e.g. Gizon, Hanasoge & Birch 2006) and numerical simulations (e.g. Baig, Dahlen & Hung 2003; Birch & Felder 2004; Birch et al. 2001; Hung, Dahlen & Nolet 2000) for simple cases. Duvall, Birch & Gizon (2006) used solar observations to construct two-dimensional travel-time kernels using small (sub-wavelength) magnetic features as point scatterers.

4.1.4 **Inversions and Resolution kernels.** Linear inversions have been developed for ring-diagram analysis and time-distance helioseismology, based on experience gained from global helioseismology (e.g., Christensen-Dalsgaard, Schou & Thompson 1990, and references therein). Two different inversion procedures are commonly used.

Let us consider 1D depth inversions for the sake of simplicity. The first inversion method, called Regularized Least Squares (RLS, e.g., Haber et al. 2000, Kosovichev 1996), is simply a fit to the observational data δd_i under conditions of smoothness. The second inversion method, called Optimally Localized Averaging (OLA, Haber et al. 2004), looks for a linear combination of the kernels (an averaging kernel) that is spatially localized around a target depth, $-z_0$. Both methods build averaging kernels of the form

$$\mathcal{K}(z; z_0) = \sum_i c_i(z_0) K_i^\alpha(z) \tag{12}$$

where the c_i are coefficients to be determined. A regularization is applied to ensure that the error on the inferred q_α is not too large, or that q_α is smooth. In addition, the cross-talk between the inferred q_α and all other quantities q_β, $\beta \neq \alpha$, should be avoided. Inversions require a good knowledge of the noise covariance matrix of the measurements, which can be estimated directly form the data (spatial averaging) or from a model (Gizon & Birch 2004).

The RLS and OLA methods give similar answers, although the RLS averaging kernels are perhaps more likely to have undesired sidelobes near the surface (Haber et al. 2004). **Figure 9** shows example RLS averaging kernels for ring-diagram analysis, in the near-surface layers. These particular kernels are used to infer horizontal flows. Very similar averaging kernels are obtained for time-distance helioseismology (e.g. Jackiewicz, Gizon & Birch 2008).

Most time-distance inversions assume that the kernels are invariant by horizontal translation, so that the horizontal convolution of the kernels with the δq_α becomes a multiplication in Fourier space. This property is used to speed-up the inversions (Jacobsen et al. 1999).

Recent progress includes the inclusion of the Born kernels in the inversions and the noise correlations (e.g. Couvidat et al. 2005). An OLA inversion for the horizontal and vertical components of the flows was implemented by Jackiewicz, Gizon & Birch (2008), in which the Born kernels and the noise covariance matrix are both consistent with the definition of the observed travel times. We note that the vertical component of velocity has been indirectly estimated from ring-diagram inversion by requiring mass conservation (e.g. Komm et al. 2004).

4.2 Strong Perturbation Regime

The solar atmosphere is permeated by concentrations of magnetic field with strength $B > 1$ kG. This magnetic field profoundly affects the solar atmosphere as well as the solar oscillations in the upper layers (Bogdan & Cally 1995, and references therein). The effects on the waves are not small and it is formally not justified to employ a single-scattering approximation to describe them. For example, the first Born approximation is not expected to capture the interaction of f and p modes with the near-surface layers of sunspots (e.g. Gizon, Hanasoge & Birch 2006).

The Lorentz force is an additional restoring force that permits the existence of new oscillation modes. In the case of a spatially uniform model with no gravity, it is possible to identify three types of magneto-hydrodynamics (MHD) waves: the fast, slow, and Alfvén waves. In gravitationally stratified magnetized atmospheres, this classification can only be applied locally. The waves couple near the layer where the sound speed and the Alfvén speed, $a = B/\sqrt{4\pi\rho}$, are equal (e.g. Schunker & Cally 2006). In a typical sunspot, the $a = c$ surface is only a few hundred km below the quiet-Sun photosphere.

The ray approximation can be extended in order to study wave propagation in MHD problems (e.g. Schunker & Cally 2006). The magnetic field affects travel times, mode frequencies, and amplitudes. These effects depend sensitively on the geometry, in particular the angle between the incident wave vector and the magnetic field vector at the $a = c$ layer. **Figure 10** shows two example ray calculations for the case of an incoming acoustic wave approaching the solar surface from below (the magnetic field, wave vector, and gravity are in the same plane). In these two calculations all of the parameters are the same except that the angle of the magnetic field has been changed. In **Figure 10*a***, the wavevector of the acoustic wave is nearly aligned with the magnetic field at the $a = c$ layer. In this case, most of the energy is transmitted to the acoustic (slow) mode of the $a > c$ region. This acoustic mode escapes along the magnetic field lines (ramp effect). Some energy is, however, converted to the fast (magnetic) mode which is then refracted by the increase of the Alfvén speed with height. In **Figure 10*b***, the incident wavevector makes a large angle with the magnetic field. At the $a = c$ level, the acoustic wave converts mostly into a magnetic (fast) mode that is refracted back into the Sun and then mostly becomes a downward propagating magnetic (slow) mode, while a small fraction of energy continues as a fast mode. The slow mode is not seen again at the surface, and thus removes energy from the surface wavefield. **Supplemental Movies 3 − 6** illustrate generalized ray theory for various values of the attack angle between the wave vector and the magnetic field. We note that in three dimensions, where the magnetic field, wave vector, and gravity are not all co-planar, strong coupling to the Aflvén wave also occurs (Cally & Goossens 2008).

Numerical simulations are an important tool to study waves in magnetized regions and sunspots. Two different approaches are employed. The first approach is numerical simulations of wave propagation through prescribed background models (e.g. Cally & Bogdan 1997; Cameron, Gizon & Daiffallah 2007; Hanasoge 2008; Khomenko & Collados 2006; Parchevsky & Kosovichev 2009). This approach permits the study of wave propagation without the complications of solving for convection and it gives the freedom to choose various background models. Typically, these codes solve the equations of motion for small-amplitude waves. The second approach is realistic numerical simulations of magnetoconvection (e.g. Rempel et al. 2009). Such simulations include self-excited waves and aim at simulating realistic solar active regions. This approach is very promising, but computer intensive.

Figure 11 shows an example calculation of the propagation of a p_1 wave packet through a simple sunspot model using the three-dimensional code of Cameron, Gizon & Daiffallah (2007). This example shows that the transmitted wave packet is phase-shifted by the sunspot (increased effective wave speed) and has a reduced amplitude compared to the quiet-Sun value. Also seen is the partial conversion of incoming p modes into downgoing slow modes. This process is responsible for absorption of acoustic energy by sunspots (Cally & Bogdan 1997, Crouch & Cally 2005, Spruit & Bogdan 1992, and Section 6). An f mode wave packet is affected in a similar fashion (Cally & Bogdan 1997; Cameron, Gizon & Duvall 2008).

The problem of inferring the subsurface structure and dynamics of solar active regions is a difficult one. In principle, standard linear inversions cannot be used because surface magnetic perturbations are not small with respect to a quiet Sun reference model. No non-linear inversion has been implemented yet. Instead there have been attempts to construct simple parametric models of magnetic regions, which have a helioseismic signature that is consistent with the observations. This approach does not require that perturbations be small. Forward models of sunspots have been proposed by, e.g., Crouch et al. (2005) and Cameron, Gizon & Duvall (2008); they will be discussed in more detail in Section 6.4.

Now that we have some understanding of the methods of local helioseismology and their diagnostic potential, we turn to a description of the main observational results: near-surface convection (Section 5), sunspots (Section 6), extended flows around active regions (Section 7), global scales (Section 8), farside imaging (Section 9), and flare-excited waves (Section 10).

5 NEAR-SURFACE CONVECTION

5.1 Supergranulation and Magnetic Network

Solar supergranules are horizontal outflows with a typical size of 30 Mm, outlined by the chromospheric network (e.g. Leighton, Noyes & Simon 1962). They have horizontal velocities of order 200 $\mathrm{m\,s^{-1}}$and lifetimes of one to two days.

Duvall et al. (1997) found that p-mode travel times contain information at supergranular length scales (**Figure 7**). As a demonstration of this, the line-of-sight component of velocity, estimated from the travel times assuming that vertical motions are negligible, was found to be highly correlated with the time averaged Dopplergram, thus confirming that local helioseismology is capable of probing convective flows at supergranulation length scales. Duvall & Gizon (2000) extended the analysis to f modes to infer horizontal flows within 2 Mm below the surface. Because they propagate horizontally, f modes are well suited to measure horizontal flows and their horizontal divergence. The flows from f-mode time-distance helioseismology compare well with flows estimated from local correlation tracking of mesogranulation (De Rosa, Duvall & Toomre 2000). Recently, Woodard (2009) has shown that direct modeling can be used to detect convection on scales of space and time that are smaller than those of supergranulation.

Figure 12 shows the most recent inversion of travel-times (Jackiewicz, Gizon & Birch 2008) using modes f through p_4. This inversion incorporates a full treatment of finite-wavelength effects (first-order Born approximation), modeling of the details of the measurement procedure, and a treatment of the statistical properties of noise. The vector flow field, averaged over $T = 3$ days, is dominated by long-lived supergranules. As seen in the figure, the divergent flows are co-spatial with upflows with about 30 $\mathrm{m\,s^{-1}}$rms velocity (with maximum values of ~ 50 $\mathrm{m\,s^{-1}}$). Near the surface, the vertical velocity can be measured in supergranules with a noise level of about 10 $\mathrm{m\,s^{-1}}$for 24 hr averages and a horizontal resolution of about 10 Mm. Estimates of the vertical velocity in supergranules from direct Doppler measurements can only be obtained near disk center and are in the range $10-30$ $\mathrm{m\,s^{-1}}$(Hathaway et al. 2002, and references therein), which is consistent with the results of local helioseismology.

Because noise reduction requires time averaging, the finite lifetime of supergranulation implies a strict limitation on the maximum depth at which we can probe the flow field before it evolves substantially. Using the f and p_1–p_4 modes, Woodard (2007) found that random noise dominates below about 4 Mm. Probing supergranules at greater depth involves statistical analysis over large fields of view and many supergranulation lifetimes in order to reduce the noise: this allows the study of the average properties of the flows at depth. Inversions of convective flows tens of Mm below the surface are challenging as they require excellent models of the sensitivity of travel times to subsurface flows (see Braun & Lindsey 2003, for a discussion) and claims of the detection of a supergranulation return flow are apparently inconsistent (e.g. Duvall 1998, Zhao & Kosovichev 2003).

The pattern of divergent flows in the surface layers is outlined by a network of small magnetic features (see Braun & Lindsey 2003, Duvall & Gizon 2000, and **Supplemental Movie 7**). This can be understood as the magnetic field is swept by the flows and concentrates at the boundaries of supergranules (e.g. Galloway, Proctor & Weiss 1977). The connections between the magnetic network and the propagation behavior of acoustic waves in the solar chromosphere can be studied by cross-correlating the observations of solar oscillations at multiple heights in the solar atmosphere (Finsterle et al. 2004b). Jefferies et al. (2006) showed that inclined magnetic field lines at the boundaries of supergranules provide 'portals' through which low-frequency (< 5 mHz) slow MAG waves can propagate up into the solar chromosphere (see **Figure 13**). This is because the cut-off frequency is lowered in the magnetic network relative to the quiet Sun by a factor $\cos\theta$, where θ is the inclination of the magnetic field to the vertical. These low-frequency upward traveling waves have been suggested to act as a source of heating of the quiet-Sun chromosphere – as an alternative to Joule heating due to magnetic field reconnection or mechanical heating due to high-frequency waves.

5.2 Rotation-Induced Vorticity

Rotation is expected to have a small effect on the dynamics of the supergranulation through the Coriolis force. As solar convection is highly turbulent, this effect can only be studied in a statistical sense using several months of data. For example, in the northern hemisphere, divergent flows are expected to have a slight positive correlation with clockwise vertical vorticity. Duvall & Gizon (2000) and Gizon & Duvall (2003) used time-distance helioseismology to make the first measurement of this small effect. After removing the average rotation and meridional circulation from the inferred flows, Gizon & Duvall (2003) studied the relationship between the horizontal divergence of the flows, denoted by 'div', and the vertical component of vorticity, denoted by 'curl'. **Figure 14*a*** shows the latitudinal dependence of $\langle\mathrm{curl}\rangle_+$ and $\langle\mathrm{curl}\rangle_-$, respectively defined as the averages of the curl over regions of positive and negative div. In the northern hemisphere, diverging flows preferentially rotate clockwise, whereas converging flows preferentially rotate counter-clockwise. This pattern is reversed in the southern hemisphere. This situation is an expected consequence of the Coriolis force. Furthermore, the latitudinal dependence of $\langle\mathrm{curl}\rangle_+$ and $\langle\mathrm{curl}\rangle_-$ are observed to be nearly exactly proportional to the radial component of the solar angular velocity, $\sin(\lambda)\Omega(\lambda)$, where λ is latitude and Ω is the solar angular velocity.

Figure 14*b* shows that the average of the product of div by curl is given by

$$\langle\mathrm{div}\,\mathrm{curl}\rangle \simeq -3\times10^{-10}\ \sin(\lambda)\Omega(\lambda)/\Omega_{\mathrm{eq}}\ \mathrm{s}^{-2}\ , \tag{13}$$

where Ω_{eq} is the equatorial angular velocity. Simple dimensional analysis of the equations of motion predicts that $\langle\mathrm{div}\,\mathrm{curl}\rangle \sim -\mathrm{Co}(\lambda)/\tau^2$ where $\mathrm{Co}(\lambda) = 2\tau\Omega(\lambda)\sin(\lambda)$ is the local Coriolis number and τ is the characteristic correlation time of the turbulence. For example, $\tau = 2$ days implies $\mathrm{Co}(\lambda)/\tau^2 \sim$

$3 \times 10^{-11} \sin(\lambda)\Omega(\lambda)/\Omega_{\rm eq}$ $\rm s^{-2}$. It is not clear if this difference of a factor of ten indicates missing physics or simply reflects the uncertainty in such estimates. Attempts at improved quantitative results suffer from arbitrarily tunable parameters.

Cyclonic convection is a means to generate poloidal field from toroidal field and is thus important in many dynamo models (for a recent review see Charbonneau 2005). In these models, the sign of the kinetic helicity $\mathcal{H}_{\rm kin} = \langle \mathbf{u} \cdot (\nabla \wedge \mathbf{u}) \rangle$ determines the strength (and sign) of this effect. Helioseismic measurements imply that the kinetic helicity at supergranulation scales is negative in the northern hemisphere (and positive in the south). This is an estimate rather than a direct measurement because the horizontal components of the vorticity have not yet been measured directly.

5.3 Evolution of Supergranulation Pattern

Gizon, Duvall & Schou (2003) studied the Fourier spectrum of long time series of maps of the horizontal divergence of the flows at supergranulation scales, measured using f-mode time-distance helioseismology. The observations reveal surprising characteristics: the signal has wavelike properties (period around 6 days) and power is anisotropic (excess power in the prograde and equatorward directions). These observations have been confirmed independently by Zhao (private communication) and Braun (private communication) using p-mode helioseismology. The power peaks at a non-zero frequency that increases slightly with horizontal wavenumber. Measurements of the Doppler shift of this apparent dispersion relation has provided a robust method for measuring the rotation and meridional flow of the solar plasma (Gizon, Duvall & Schou 2003; Gizon & Rempel 2008). An interesting aspect of this work is that the inferred rotation and the meridional flow match the motion of the small magnetic features (e.g. Komm, Howard & Harvey 1993a,b). On the other hand, correlation tracking measurements applied to the divergence maps overestimate rotation and underestimate the meridional flow by large amounts (see Gizon & Birch 2005). The time evolution of the supergranulation pattern does not reflect its advection by the plasma flow, although the two can be decoupled in Fourier space.

We note that Hathaway, Williams & Cuntz (2006) demonstrated that the local correlation tracking of Doppler features on the Sun gives biased estimates of the rotation rate because of line-of-sight projection effects. This case, however, is not directly comparable to the observations described above since helioseismic divergence maps are not expected to be sensitive to line-of-sight projection effects at supergranulation scales.

The helioseismic observations of the wavelike properties of supergranulation are still calling for an explanation. Supergranulation may perhaps be related to the traveling convection modes seen in idealized systems with rotation (e.g. Busse

2007).

6 SUNSPOTS

In this section we discuss inferred flows in the immediate vicinity of sunspots (Section 6.2), the absorption of waves by sunspots (Section 6.3), and the subsurface structure of sunpots (Section 6.4). Recent reviews about sunspots are provided by, e.g., Solanki (2003) and Moradi et al. (2009, submitted).

The absence of a sufficiently conclusive theory has allowed a wide range of ideas about the origin and structure of sunspots to develop. These range all the way from intuitive ideas directly inspired by the abundant observational clues, to mathematically oriented ones that require ignoring almost all of these clues. Some of the ideas should become testable if they make relevant predictions for the relatively shallow layers below the surface that are accessible to local helioseismology methods.

6.1 The Anchoring Problem

The magnetic forces exerted by the spot on its surroundings are significant. If it were not in a quasi-stable equilibrium in its observable layers, a spot would evolve on the time for the Alfvén speed to cross the size of the spot (on the order of an hour), much shorter than the observed life times of spots (days to weeks). The magnetic forces also make the sunspot plasma buoyant. Together, this gives rise to an 'anchoring problem' (cf. Parker 1979). A sunspot cannot be just a surface phenomenon since magnetic field lines have no ends. The sunspot's field lines continue below the surface. In contrast with a scalar field like pressure, the magnetic field of a sunspot cannot be kept in equilibrium simply by pressure balance at the surface: the tension in the magnetic field lines continuing below the surface exerts forces as well. The magnetic tension acting at the base of the spot keeps it together and prevents buoyancy from spreading it like an oil slick over the solar surface. Sunspots also rotate faster than the solar surface, indicating that they sense the increase of rotation with depth.

The question of sunspot equilibrium thus involves deeper layers, down to wherever the field lines continue. At which depth and by which agent is the sunspot flux bundle kept together? A very stable location is the boundary of the convection zone with the stably stratified radiative interior of the Sun. A layer of magnetic field floating on this boundary becomes unstable only at a field strength of about 10^5G (Schüssler et al. 1994). The existence of such a critical field strength was hypothesized by Babcock (1961). The subsequent rise to the surface is what creates the observed bipolar active regions, as proposed by Cowling (1953). The action of the Coriolis force on flows in the magnetic field associated with the instability produces the poloidal field of the next cycle, and is observable on the surface in the form of the systematic tilt of active region axes with respect to the azimuthal direction (Leighton 1969). A boost of confidence has been provided by recent realistic 3D radiative MHD simulations of the last stages of the emergence process of magnetic fields at the surface. These are beginning to look much like real observations (Cheung et al. 2008). Though largely qualitative, the view of the solar cycle developed by Babcock and Leighton appears to be the most fruitful frame of reference for interpreting the solar cycle.

6.2 Moat Flow

In the photosphere, sunspots are typically surrounded by diverging horizontal outflows, termed moat flows, with amplitudes of several hundred $\mathrm{m\,s^{-1}}$. These outflows typically extend to about twice the radius of the penumbra. Moat flows were first detected using direct Doppler measurements (Sheeley 1972) and also can be inferred from the motion of small magnetic features (e.g. Brickhouse & Labonte 1988).

Local helioseismology is a useful tool for studying flows around sunspots (Duvall et al. 1996, Lindsey et al. 1996). Gizon, Duvall & Larsen (2000) used f-mode time-distance helioseismology to study the moat flows in the two Mm below the surface. Comparisons between the near-surface flows inferred from local helioseismology with direct Doppler measurements have demonstrated the validity of the near-surface inversions. **Figure 15** shows the moat flow at a depth of 1 Mm using a time-distance inversion and all ridges from f through p_4 (Gizon et al. 2009). At this depth, the moat flow has an amplitude of $\sim 250\ \mathrm{m\,s^{-1}}$, which is consistent with the motion of the small magnetic features. This outflow is detected in the top 4 Mm. Such measurements of the subsurface moat flow have been confirmed by ring-diagram analysis (Moradi et al. 2009, submitted).

The moat flow is believed to be driven by a pressure gradient caused by the blockage of heat transport by sunspots (e.g. Nye, Bruning & Labonte 1988). For a more accurate description in terms of the surface cooling that causes the observed flows, see Spruit (1997). Though much slower, the moat flow appears physically connected with the Evershed flow in the penumbra. This is evident both from the observations by, e.g., Cabrera Solana et al. (2006) and the realistic numerical simulations of Heinemann et al. (2007) and Rempel et al. (2009).

6.3 Absorption of Solar Oscillations

The first major discovery made by local helioseismology was that solar oscillations (f and p modes) are absorbed by sunspots (Braun, Duvall & Labonte 1987). This discovery was made using Fourier-Hankel analysis, which is based on the decomposition of the wavefield around the sunspot into ingoing and outgoing waves. Braun, Duvall & Labonte (1987, 1988) found that typical sunspots can absorb up to 50% of the incoming power.

Spruit & Bogdan (1992) proposed that mode conversion between the oscillations of the quiet Sun and the slow magneto-acoustic waves of the sunspot could explain the observations of wave absorption by sunspots. Theoretical modeling (Cally & Bogdan 1993, Crouch et al. 2005) and numerical simulations (Cally 2000; Cally & Bogdan 1997; Cameron, Gizon & Duvall 2008) demonstrated that mode conversion is indeed capable of removing a large fraction of the energy from the helioseismic waves incident on a sunspot. The efficiency of the mode conversion is strongly dependent on the angle of the magnetic field from the vertical, with a maximum in the absorption occurring at an angle of about 30° from the vertical (Cally, Crouch & Braun 2003). Comparisons between observations and models (e.g. Cameron, Gizon & Duvall 2008; Crouch et al. 2005) show that the explanation of mode conversion is consistent with the observations of the reduction of outgoing wave power. We note that plage regions are also known to 'absorb' incoming waves.

6.4 Phase Shifts and Wave-Speed Perturbations

Fourier-Hankel analysis (Section 3.6) has demonstrated that outgoing waves from sunspots have different phases than the corresponding ingoing waves (Braun 1995, Braun et al. 1992). At fixed radial order, the phase shifts increase roughly linearly with increasing angular degree. Fan, Braun & Chou (1995) used a simple model, in which the sunspot is treated as a local enhancement in the sound-speed, to suggest that these phase shifts are indicative of a near-surface change in the wave speed relative to quiet Sun. Crouch et al. (2005) showed that approximate models of wave propagation in a model sunspot (embedded magnetic cylinders) could simultaneously explain the absorption and phase shift measurements. The success of these simple models suggests that the interaction of solar oscillations with the sunspot magnetic fields may be the essential physics in understanding both wave absorption (Section 6.3) and the phase shifts caused by sunspots.

Time-distance, holography, and ring-diagrams have all been used to infer changes in the wave speed in sunspots (e.g. Basu, Antia & Bogart 2004; Couvidat, Birch & Kosovichev 2006; Jensen et al. 2001; Kosovichev 1996; Kosovichev, Duvall & Scherrer 2000, among a great many others). Interpretation of the helioseismic measurements is a rapidly developing topic of current research. Figure 16 shows a comparison between time-distance and ring-analysis inversions, forward models based on Fourier-Hankel analysis, and a realistic numerical simulation of a sunspot. As was shown by Gizon et al. (2009) and Moradi et al. (2009, submitted), there is not yet agreement among the different analysis methods, especially between the time-distance and ring-diagram results. There are a number of possible explanations for this disagreement. Current inversions for the time-distance and ring-diagram methods use sensitivity functions that do not explicitly include the direct effects of the magnetic field and both assume that wave-speed perturbations are small. The time-distance sensitivity functions may not model the reference power spectrum sufficiently accurately (convective background, mode frequencies, relative mode amplitudes, line widths and asymmetries). Neither method fully accounts for the details of the measurements procedure, especially in the case of time-distance where the effects of the data analysis filtering in Fourier space (e.g., phase-speed filters) are not fully accounted for. Except for the time-distance inversion, all other methods are consistent with an increased wave speed in the top 2 Mm and show wave-speed perturbations with amplitudes less than about 2% at greater depths.

Direct simulation of wave propagation through sunspot models is useful to test the validity of these models. Cameron, Gizon & Duvall (2008) used a three-dimensional MHD code to compute the propagation of f modes through a model sunspot. Here we show a computation for the propagation of a p_1 wave packet using the same simulation code. The simulated wavefield, solution to an initial value problem, is compared to the observed cross-covariance in **Figure 17** in order to assess the validity of the underlying sunspot model. Like for the f modes, the comparison with the observations is promising: the amplitude of the transmitted waves is reduced and the waves travel faster in the sunspot than in quiet Sun.

As mentioned in Section 4.2, sunspot magnetic fields strongly affect the nature of the wave properties in the surface layers. In particular, upward propagating high-frequency ($\omega > \omega_{\mathrm{c}}$) waves are reflected and refracted at the $a = c$ surface, where MHD mode conversion occurs. Finsterle et al. (2004b) used multi-height observations of solar oscillations to map the $a = c$ surface in active regions, called the 'magnetic canopy'. The travel time measured between two observation heights in the solar atmospheres was used to derive the propagation properties of the waves between these two layers. When both heights are above the $a = c$ layer, waves are evanescent and the travel time vanishes. Using combinations of three heights, they find that in sunspots and active regions the canopy deeps below the base of the photosphere by several hundred km, while it is above 1000 km in the quiet Sun.

7 EXTENDED FLOWS AROUND ACTIVE REGIONS

In this section, we describe flows around large complexes of magnetic activity. These flows should not be confused with the (smaller scale) moat flow around individual sunspots, which was discussed in Section 6.

7.1 Surface Inflows, Deeper Outflows

Using f-mode time-distance helioseismology, Gizon, Duvall & Larsen (2001) detected weak $\sim 50\ \mathrm{m\,s^{-1}}$surface flows that converge toward active regions (**Figure 18**). These inflows, which exist as far as 30° from the centers of active regions, are also seen in ring diagram analyses (e.g. Haber et al. 2001, 2004, Komm et al. 2007). In fact, Hindman et al. (2004) showed that the time-distance and ring-diagram methods give nearly identical results near the surface. These near-surface flows also agree reasonably well with the motion of supergranules (Švanda, Zhao & Kosovichev 2007). The converging flows near the surface are accompanied by cyclonic flows with vorticity of order $10^{-7}\ \mathrm{s^{-1}}$ (Komm et al. 2007).

At depths in the range of about 10 Mm to 15 Mm, diverging flows from active regions have been inferred using the time-distance (Zhao & Kosovichev 2004) and ring-diagram (Haber et al. 2004) methods. These diverging flows typically have amplitudes of order $50\ \mathrm{m\,s^{-1}}$. Komm et al. (2004) used ring-diagram measurements together with the constraint of mass conservation to infer downward flows of order $1\ \mathrm{m\,s^{-1}}$, at depths less than about 10 Mm, in and around active regions. Below this depth, the active regions tend to show upflows.

The observations are summarized in **Figure 19**, which shows the organization of horizontal flows around a particular complex of magnetic activity at three different depths. The flow patterns are consistent from day to day, despite the presence of supergranulation noise.

7.2 Flows due to Thermal Effects of Magnetic Fields

A diagnostically important class of flows are those associated with thermal effects due to magnetic fields, such as heating by dissipation of magnetic energy or the enhanced radiative loss of small scale magnetic fields at the surface. On intermediate to large scales and time scales exceeding the rotation period approximate geostrophic balance holds in the convection zone. Hence flows of the thermal wind type must accompany thermal disturbances on those scales. For example, the enhanced radiative loss from the small scale magnetic field in active regions has a cooling effect that should drive an inflow at the surface and a circulation in the cyclonic sense around the active region (Spruit 2003), as in low pressure systems in the Earth's atmosphere. This may be an explanation for the flows described in the previous section.

8 GLOBAL SCALES

The dominant global-scale flows in the Sun are the differential rotation and the meridional flow. Helioseismic measurements made over long time scales (a few solar rotation periods) effectively remove the contribution of small-scale convective flows and active region flows and allow high precision studies of these global-scale flows. Both rotation and the meridional flow show small variations with the solar cycle.

8.1 Differential Rotation

The North-South symmetric component of internal differential rotation has been measured using global helioseismology (cf. review by Thompson et al. 2003). The solar rotation rate depends strongly on latitude in the convection zone, with the equator rotating more quickly than the poles. The rotation rate shows only a weak radial shear in the bulk of the convection zone. There is strong radial shear in the very near surface layers (top 35 Mm, Schou et al. 1998), and in the tachocline where the differentially rotating convection zone meets the uniformly rotating radiative zone. The tachocline plays an important role in most dynamo theories of the solar cycle.

As the differential rotation is well known, it provides an important test of local helioseismic methods. Giles, Duvall & Scherrer (1998) measured rotation with time-distance helioseismology applied to MDI data and found good qualitative agreement with the results of global helioseismology. Basu, Antia & Tripathy (1999) and González Hernández et al. (2006) both used ring-diagram analysis to study the differential rotation in the near-surface shear layer. These studies found rotation rates that essentially agreed with those inferred from global helioseismology in the top 20 Mm (increasing angular velocity with depth), below that depth the measurements showed instrument dependent systematic errors.

8.2 Meridional Flow

Doppler measurements (e.g. Hathaway 1996) reveal a surface meridional flow with an amplitude of about 20 $\mathrm{m\,s^{-1}}$from the equator to the poles. It has also been measured by tracking magnetic elements (Komm, Howard & Harvey 1993a), with essentially the same result. This surface meridional flow implies a subsurface return (i.e., equatorward) flow.

In flux-transport dynamo models (e.g. Charbonneau 2005, Dikpati & Charbonneau 1999), the meridional flow is responsible for the redistribution of flux from the active latitudes to the poles (at the surface) and in some models also from the poles to equator (at the base of the convection zone). Hathaway et al. (2003) argued that the equatorward drift of sunspots during the course of the solar cycle (the butterfly diagram) implies the existence of a 1.2 $\mathrm{m\,s^{-1}}$return flow at the bottom of the convection zone. However Schüssler & Schmitt (2004) argue that the butterfly diagram could be reproduced by a traditional model of dynamo waves without transport of magnetic flux by a flow.

In addition to its role in some dynamo theories, the meridional flow is also thought to play an important role in transporting angular momentum and thus in maintaining the differential rotation (for a recent review see Miesch 2005).

The meridional flow produces a second-order shift in the frequencies of the global modes (unlike, for example, the differential rotation which produces a first-order shift) and is therefore very difficult to measure using traditional global helioseismology. The meridional flow does however produce a first-order change in the eigenfunctions of the modes of the Sun, and thus produces first-order effects in local helioseismic measurements.

Giles et al. (1997) used time-distance helioseismology to obtain the first detection of the subsurface meridional flow. Imposing a mass conservation constraint, inversions of the time-distance measurements suggested a meridional flow that fills the convection zone, is equatorward below about $0.8R_\odot$, and has a strength of about 2 $\mathrm{m\,s^{-1}}$at the base of the convection zone (Giles 2000). These deep results, however, are not direct measurements.

Figure 20 shows measurements of the meridional flow close to the surface, using ring-diagram analysis and (a variant of) time-distance helioseismology. The maximum amplitude of the meridional flow is about 15–20 m/s. The eleven years of data show that the meridional flow varies significantly (up to 50% of its mean value). The solar-cycle dependence of the meridional flow will be discussed in the next section.

As discussed by Braun & Birch (2008), one of the fundamental difficulties in measuring the deep meridional flow is that the noise level, due to the stochastic nature of solar oscillations, is very large compared to the weak signal expected from a flow of a few $\mathrm{m\,s^{-1}}$(for comparison, the sound speed at the base of the convection zone is roughly 230 $\mathrm{km\,s^{-1}}$).

Numerical simulations of convection in rotating shells (Miesch, Brun & Toomre 2006) have roughly reproduced the overall amplitude of the meridional flow, although in these simulations the meridional flow is highly variable and has a multiple-cell structure. These simulations rely on the presence of a small latitudinal entropy gradient to establish solar-like differential rotation as suggested by Rempel (2005). This gradient is imposed at the base of the convection zone model as an adjustable part of the boundary conditions. The differential rotation in these models is thus what in geophysics is called a 'thermal wind', much like the global atmospheric circulation on earth is due to the pole-equator temperature difference. In the Sun the cause for such latitudinal entropy variation is not quite clear, however. Independent of this unsolved question, the fact that the simulations so far appear unable to reproduce the solar differential rotation without an imposed entropy gradient is significant. It implies that models of the Sun's differential rotation based on Λ-effect or anisotropic turbulence formalisms so far are not substantiated by numerical simulations.

8.3 Solar-Cycle Variations

The time varying component of rotation shows bands of slower and faster rotation ($\pm 10\ \mathrm{m\,s^{-1}}$) that migrate in latitude with the phase of the solar cycle. This pattern, called torsional oscillations, was first seen in direct Doppler measurements (Howard & Labonte 1980). The torsional oscillations have two branches. At latitudes less than about 45°, the bands of increased and decreased rotation move towards the equator at the same rate as the active latitudes, with the active latitudes located on the poleward side of the fast band. At high latitudes, the bands move towards the poles. Global helioseismology has shown that the torsional oscillations have their maximum amplitude close to the surface, but extend throughout much of the convection zone (e.g. Vorontsov et al. 2002). The torsional oscillations tend to be roughly uniform along contours of constant rotation rate (e.g. Howe et al. 2005). As reviewed by Gizon & Birch (2005), local helioseismology has been used to confirm many of these results for the shallow component of the torsional oscillations. **Figure 21** shows the time residuals of the zonal flows near the surface (time-distance helioseismology).

In addition, local helioseismology has shown that there are fluctuations, with amplitudes of $\pm 5\ \mathrm{m\,s^{-1}}$, in the meridional flow that are associated with the butterfly diagram (this pattern was seen in direct Doppler measurements by Ulrich et al. 1988). As shown in **Figure 21**, near the surface these local fluctuations correspond to flows converging towards the active latitudes (e.g. Gizon & Rempel 2008, González Hernández et al. 2008). The exact depth where these flows change sign is not well known, but at depths of roughly 50 Mm, the component of the meridional flow associated with the torsional oscillations converges towards the active latitudes (e.g. Beck, Gizon & Duvall 2002; Chou & Dai 2001). The contribution of flows around individual active regions to the torsional oscillations and associated meridional flows will be discussed in Section 7.

Schüssler (1981) and Yoshimura (1981) suggested that the torsional oscillations may be caused by the Lorentz force associated with migrating dynamo waves. A turbulent mean field dynamo model by Covas et al. (2000), fitted to a butterfly diagram of the solar cycle, shows a Lorentz force-induced torsional oscillation pattern at the surface resembling the observations. As in other Lorentz-force models, however, its amplitude increases strongly with depth, in contrast with the helioseismic measurements. Kitchatinov et al. (1999), building on work by Küker, Rüdiger & Pipin (1996), suggested that the torsional oscillations result from the effect of the magnetic field on the convective transport of angular momentum. Another suggested explanation is the reduction of turbulent viscosity in active regions (Petrovay & Forgács-dajka 2002).

Spruit (2003) suggested that the torsional oscillations may be a result of geostrophic flows set up by enhanced surface cooling in regions of magnetic activity. Since the driving force in this explanation is at the surface, the velocity signal produced decreases with depth as observed. Rempel (2007) argued that such a thermal forcing, rather than mechanical forcing as in the Lorentz-force based models, is required to explain the observed deviation of the low-latitude torsional oscillations from a Taylor-Proudman state (zonal velocity constant on cylinders). Similarly, Gizon & Rempel (2008) suggested that the only current model for the low-latitude branch of the torsional oscillations and associated meridional flows that is qualitatively consistent with the observations is the enhanced cooling model of Spruit (2003). One complication for models that invoke thermal forcing at the surface is to explain the presence of the torsional oscillations at solar minimum (Gizon & Rempel 2008). It should be noted that the model of Rempel (2007) does not require enhanced thermal forcing at high latitudes ($> 50°$) to explain the poleward-propagating branch of the torsional oscillations. The two branches of the zonal torsional oscillations may have different physical origins.

8.4 Contribution of Active Region Flows to Longitudinal Averages

An interesting question is whether the localized flows around active regions (Section 7) contribute significantly to the solar-cycle variation of the longitudinal averages of the differential rotation and the meridional flow. The inflows/outflows around active regions could affect the average meridional circulation around the mean latitude of activity, while the vortical component of the flows could affect the average zonal flows.

In order to study this question, Gizon (2003) selected all regions within 5° of all locations with strong magnetic field and excluded these regions from the longitudinal averages of the flows. The zonal flows are essentially unaffected (except for the fact that active regions rotate a little more rapidly than quiet Sun): localized cyclonic flows around large active regions do not provide a sufficient explanation for the torsional oscillations. This is not particularly surprising since torsional oscillations exist at solar minimum, in the absence of active regions. The torsional oscillations model of Spruit (2003) would have to rely on the thermal disturbances caused by diffuse small-scale magnetic fields, not localized active regions. On the other hand, Gizon (2003) finds that the inflows around active regions appear to be largely responsible for the near-surface solar-cycle dependence of the meridional flow, at the level of a few $\mathrm{m\,s^{-1}}$. This conclusion has been challenged however by González Hernández et al. (2008), which indicates that the answer depends sensitively on the selection of the regions of activity that are removed from the longitudinal averages.

9 FARSIDE IMAGING

Lindsey & Braun (2000) introduced the concept of farside imaging, in which observations of the solar oscillations made on the visible disk are used to infer the presence of active regions on the farside of the Sun. Farside imaging has been achieved using both holography-based methods (e.g. Lindsey & Braun 2000) and time-distance helioseismology (Zhao 2007). Hartlep et al. (2008) have successfully tested farside time-distance helioseismology with numerical simulations.

The conceptual ray geometry for farside imaging is shown in **Figure 22*a***. In the 2+2 skip geometry, wave packets leave the visible surface, make two skips in the solar interior (this involves one reflection from the surface), interact with possible surface magnetic activity on the farside, make two more skips, and are then seen again on the front side. The total travel time of the wave packet is sensitive to the presence of large active regions on the farside. Travel-time reductions of up to ten seconds are typically observed for large active regions. By moving the farside target location, a map of the farside magnetic activity can be constructed. The 2+2 skip geometry is suitable for mapping regions that are not too far from the antipode of the center of the visible disk. In order to complete the farside maps, other skip geometries are required (Braun & Lindsey 2001). The 1+3 skip geometry targets active regions closer to the limb. In this geometry, the wave packets only skip once before they reach the target location, and then skip three times before they are observed again. Oslund & Scherrer (2006, unpublished) combined farside maps from the 2+2 and 1+3 skip geometries to make maps of the entire farside of the Sun. These farside maps are produced daily using the MDI/SOHO data and are available online (see **Related Resources**).

Figure 22*b* and **Supplemental Movies 9 and 10** and shows a sequence of farside maps that show a large active region moving across the farside and front-side of the Sun. This active region, NOAA 9503, was seen to form on the farside of the Sun before appearing on the visible disk about 12 days later. Magnetic maps of the farside provide up to two weeks of advance warning before large active regions rotate onto the visible disk, and thus are expected to play an important role in predicting space weather.

In order to interpret the farside maps in terms of physical variables, such as the total unsigned magnetic flux, González Hernández, Hill & Lindsey (2007) have proposed to calibrate the farside images using long lived active regions that are seen before and after they appear on the farside. Future Sun-orbiting spacecraft carrying solar and magnetic imagers (e.g., Solar Orbiter) will provide enhanced opportunities for detailed farside calibration.

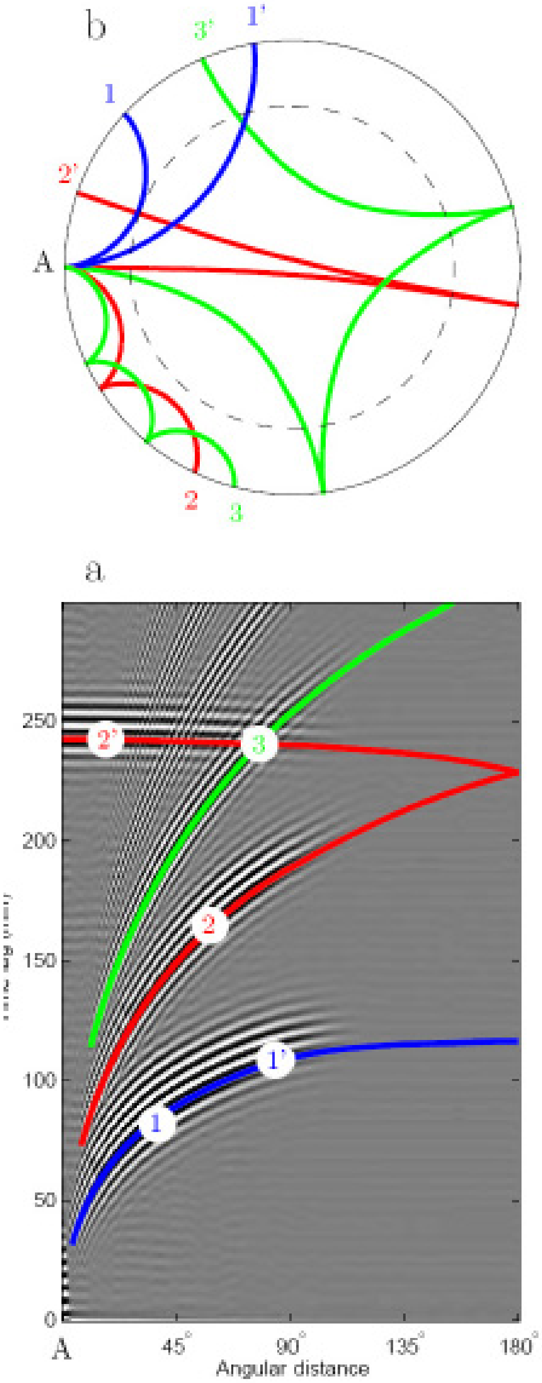

Figure 6: (*a*) Measured cross-covariance function for MDI medium-degree data as a function of separation distance and time-lag (Kosovichev, Duvall & Scherrer 2000). Positive values are white, negative values black. The observation duration is $T = 144$ days starting in May 1996. (*b*) Example ray paths for acoustic wave packets. In both panels (*a*) and (*b*) the blue lines correspond to single skip ray paths, the red lines are for two skip paths, and the green lines are for three-skip paths.

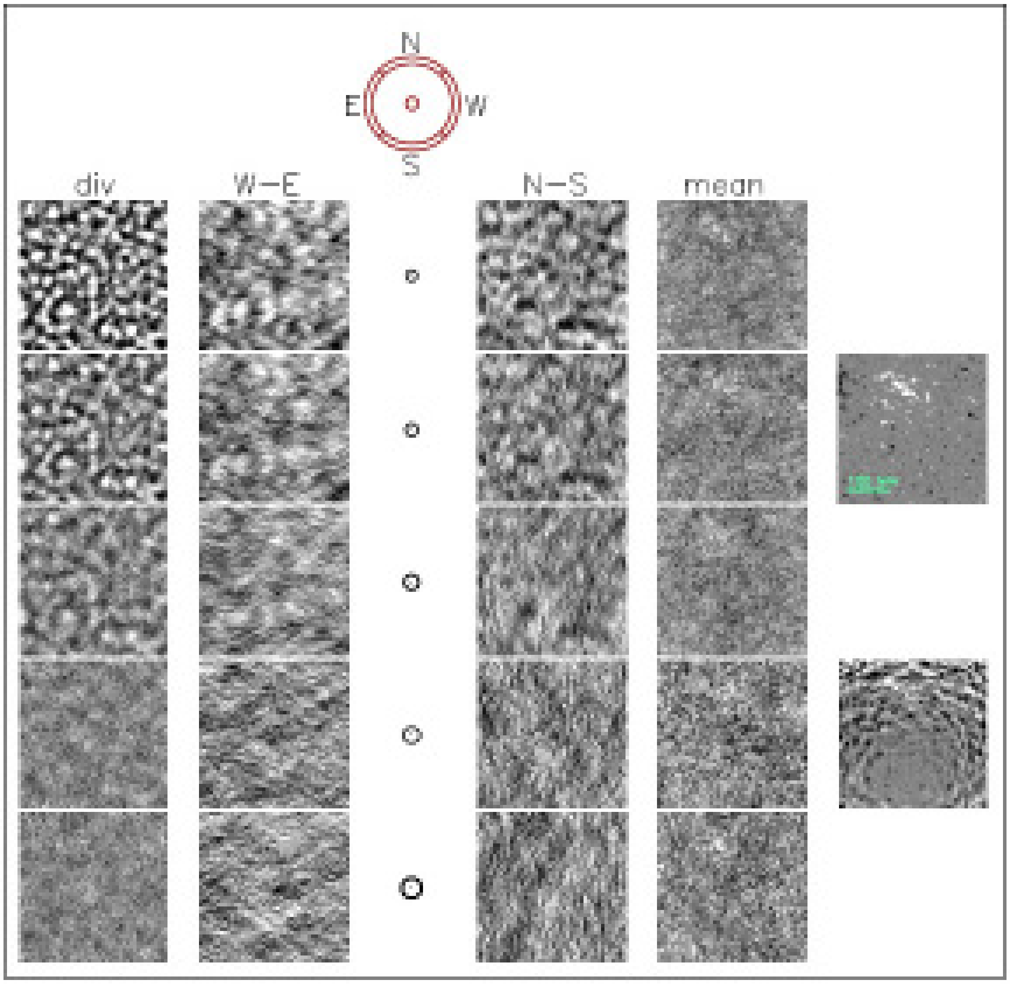

Figure 7: Maps of the travel times using the annulus/quadrant geometry and MDI/SOHO high-resolution data (Duvall et al. 1997). The observation duration is $T = 8.5$ hr. Each frame is 370 Mm on a side. Each row corresponds to a different annulus radius from 12 Mm to 27 Mm. The columns show the four types of travel-time measurements. From left to right: (i) travel-time difference between the outward-going waves and the inward-going waves, (ii) travel-time difference between the westward- and eastward-going waves, (iii) travel-time difference between the northward- and southward-going waves, and (iv) mean of the travel times of the inward- and outward going waves. The average magnetogram and the average Dopplergram are shown in the right most column. The travel-time perturbations are mostly due to the supergranular scale horizontal flows.

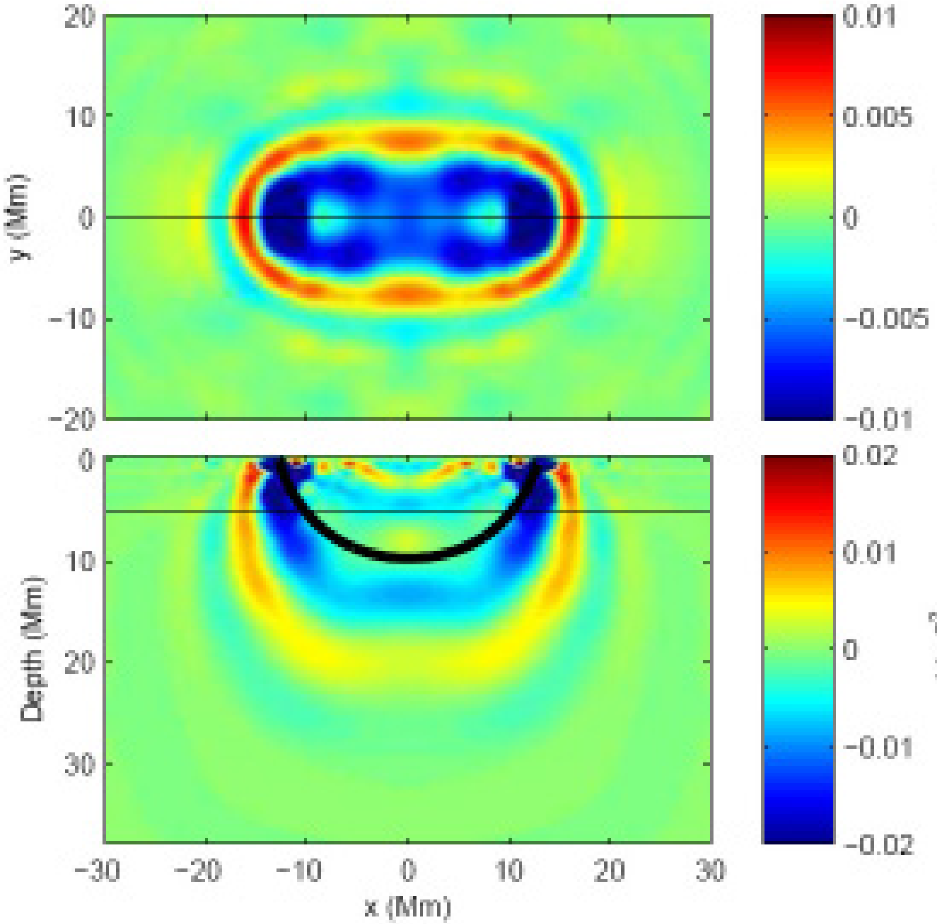

Figure 8: Linear sensitivity of a single-skip mean travel-time shift to local changes in the square of the sound speed. The observation points are located at $(x, y, z) = (\pm 12.5, 0, -0.2)$ Mm. The top panel shows a horizontal slice at a depth of 5 Mm. The bottom panel shows a vertical slice at $y = 0$. The heavy black line in the lower panel shows the single-skip ray path connecting the observation points. The kernel has been scaled with the background speed to enhance the visibility of the subsurface structure. The ringing away from the ray path is due to the band-limited nature of solar oscillations. The linear sensitivity is almost zero along the ray path, this a generic feature of sound-speed kernels in three dimensions, and is well known in seismology (Dahlen, Hung & Nolet 2000; Marquering, Dahlen & Nolet 1999).

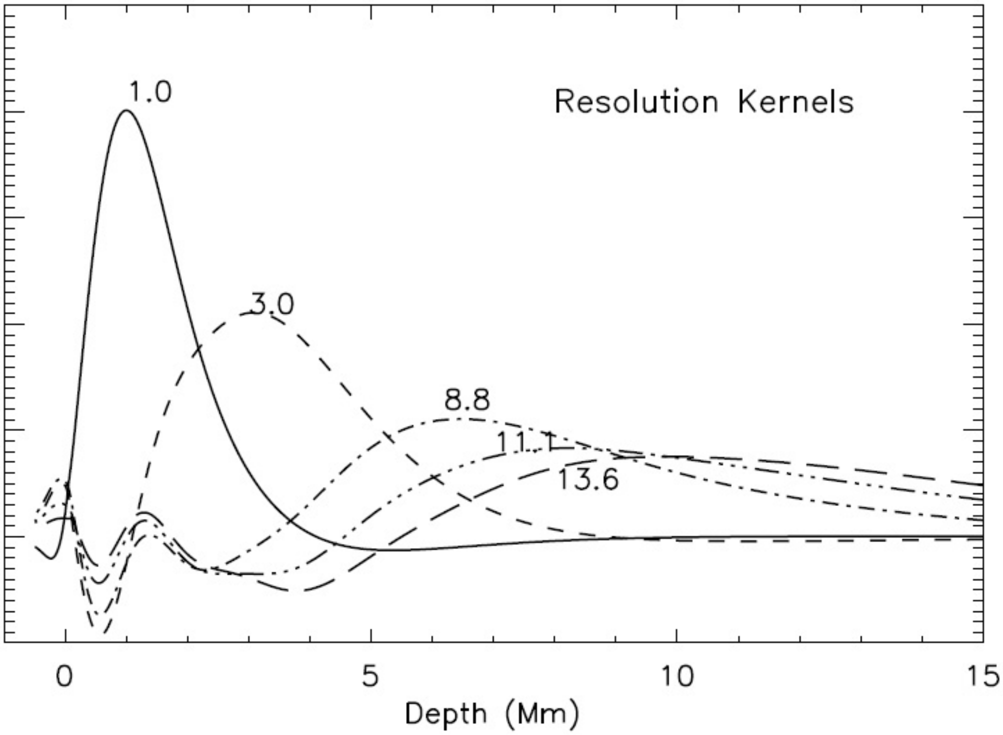

Figure 9: Averaging kernels, $\mathcal{K}$, from 1D RLS inversions for ring-diagram analysis (depth sensitivity to horizontal flows). The numbers (in units of Mm) refer to the average depths of the averaging kernels. Courtesy of Irene González-Hernández.

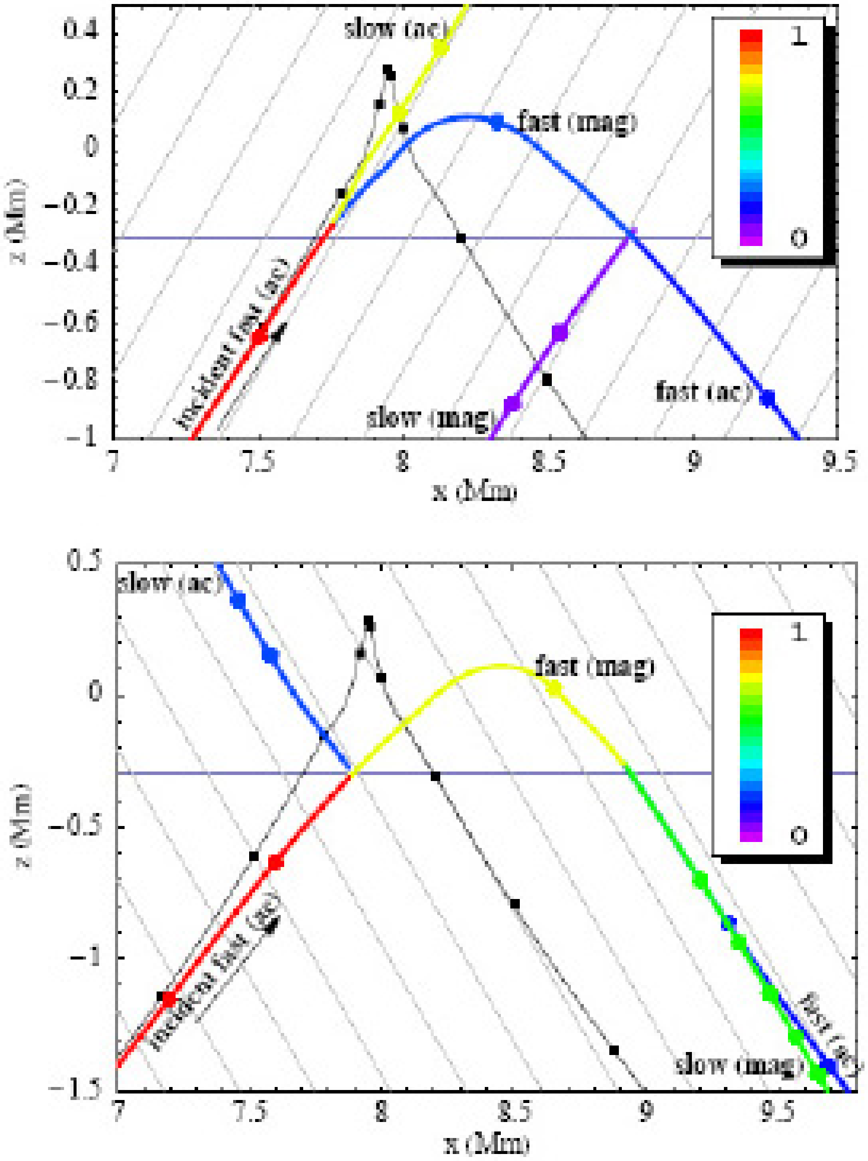

Figure 10: Ray paths in model surface layers with 2 kG uniform magnetic field inclined at ±30° respectively to the vertical, as shown by the background gray lines. The incoming 5 mHz rays (arrows) have lower turning points at $z = -5$ Mm and are shown in red. The two frames correspond to two different attack angles. The horizontal gray line indicates where the sound speed and the Alfvén speed coincide, which is approximately where mode conversion happens. The fractional energy remaining in each resulting ray is indicated by the color legend. The dots on the ray paths indicate 1 min group travel time intervals. The thin black curve represents the acoustic ray that would be there in the absence of magnetic field. Note that the fast ray is faster through the surface layers than the non-magnetic ray. Figure and caption from Cally (2007). Figure copyright *Wiley-VCH Verlag GmbH & Co. KGaA*. Reproduced with permission.

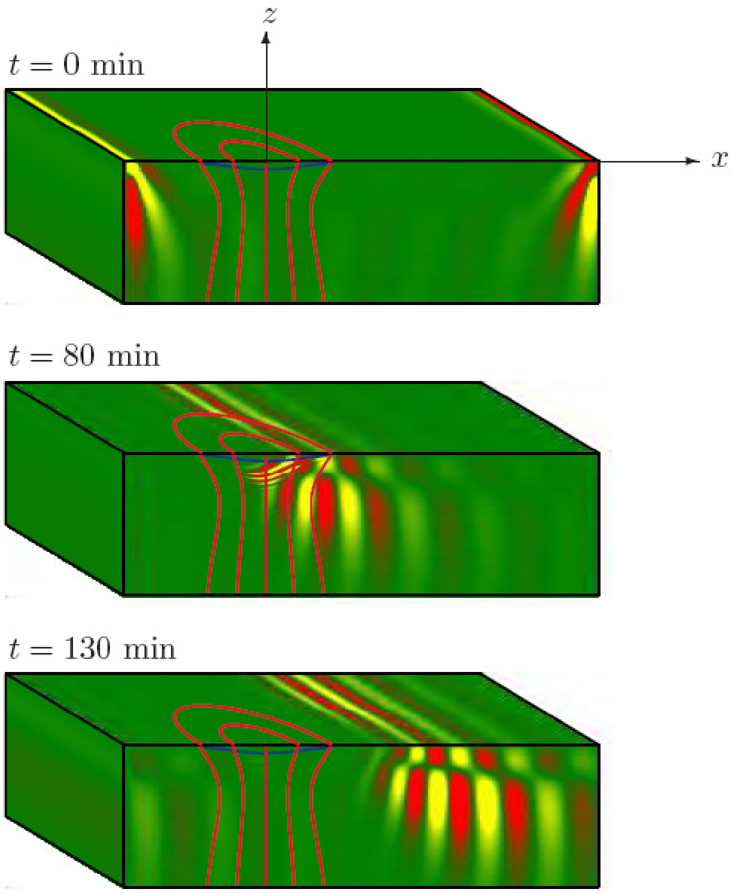

Figure 11: Numerical simulation of the propagation of a p_1 plane wave packet through a model sunspot using the MHD code of Cameron, Gizon & Daiffallah (2007). The sunspot model is similar to the model of Schlüter & Temesváry (1958) with a maximum vertical field $B_z = 3$ kG at the surface; it is embedded in a Model S background atmosphere, stabilized with respect to convection. The wave packet is initially located 40 Mm to the left of the sunspot and propagates to the right. The x-component of velocity is shown at times $t = 0$, 80, and 130 min (positive values in red, negative values in yellow). The $a = c$ level is represented by the blue curve. The computational domain is -40 Mm $< x <$ 105 Mm, -36.5 Mm $< y <$ 36.5 Mm and -12.5 Mm $< z <$ 1.5 Mm. Only half of the box ($y > 0$) is shown. The boundary conditions are periodic in the horizontal directions and there are two sponge layers (not shown here) at the top and at the bottom of the box to avoid the reflection of the waves back into the computational domain. The $t = 80$ min snapshot clearly shows the slow magneto-acoustic waves propagating down the sunspot. Because these slow waves are transverse, they are easily seen as oscillations in the x-component of velocity. See **Supplemental Movie 8**.

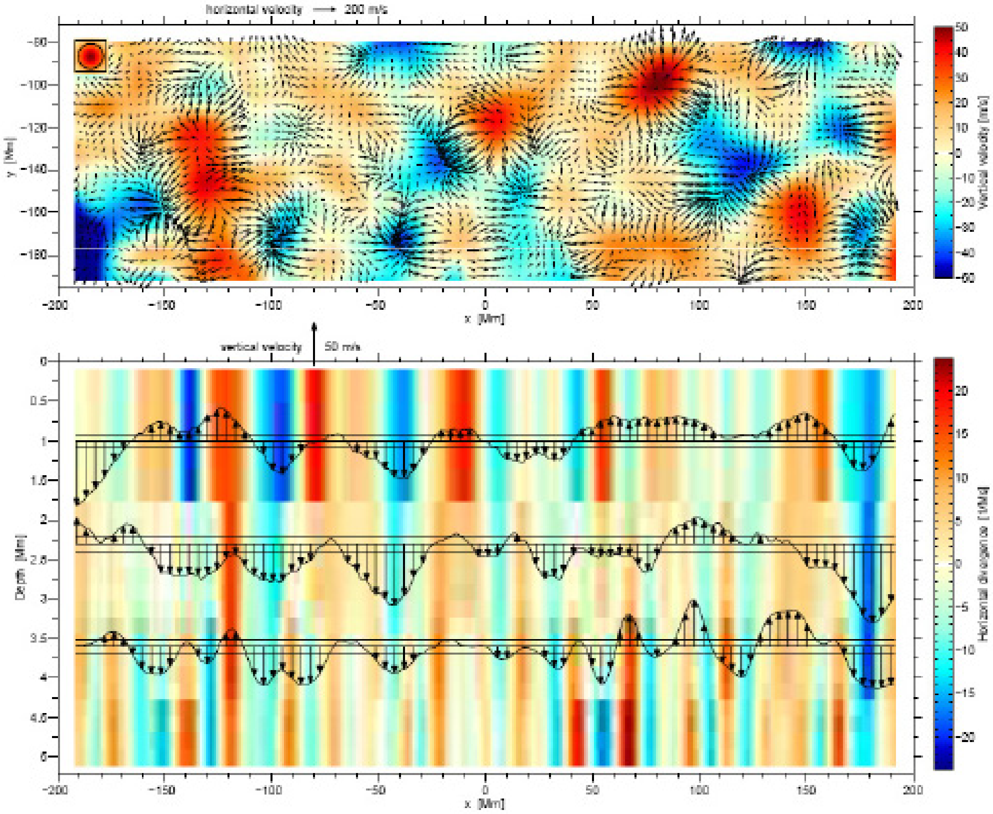

Figure 12: Inversion for vector flows in the near surface layers. The travel times were measured for ridges f and p_1 through p_4 and inverted using an OLA technique. The observation time is $T = 3$ days. *Top panel*: Horizontal slice at the depth of 1 Mm showing the two horizontal components (u_x and u_y, arrows) and the vertical component (u_z, colors) of the vector flow field. The FWHM of the averaging kernel is 10 Mm (inset in top-left corner). The most visible features correspond to long-lived supergranules. *Bottom panel*: Vertical slice at $y = -176$ Mm (white line in a) showing the horizontal divergence of the flow field as a function of x and depth (colors) from the same 2+1D inversion. The vertical arrows show the vertical velocity u_z for the three ridges f, p_1, and p_2 (from top to bottom) from a 2D horizontal inversion, plotted at the depths corresponding to the mean depth of the respective averaging kernels. The one-sigma level of random noise in u_z is equal to 10 $\mathrm{m\,s^{-1}}$by construction (horizontal black lines). Adapted from Jackiewicz, Gizon & Birch (2008).

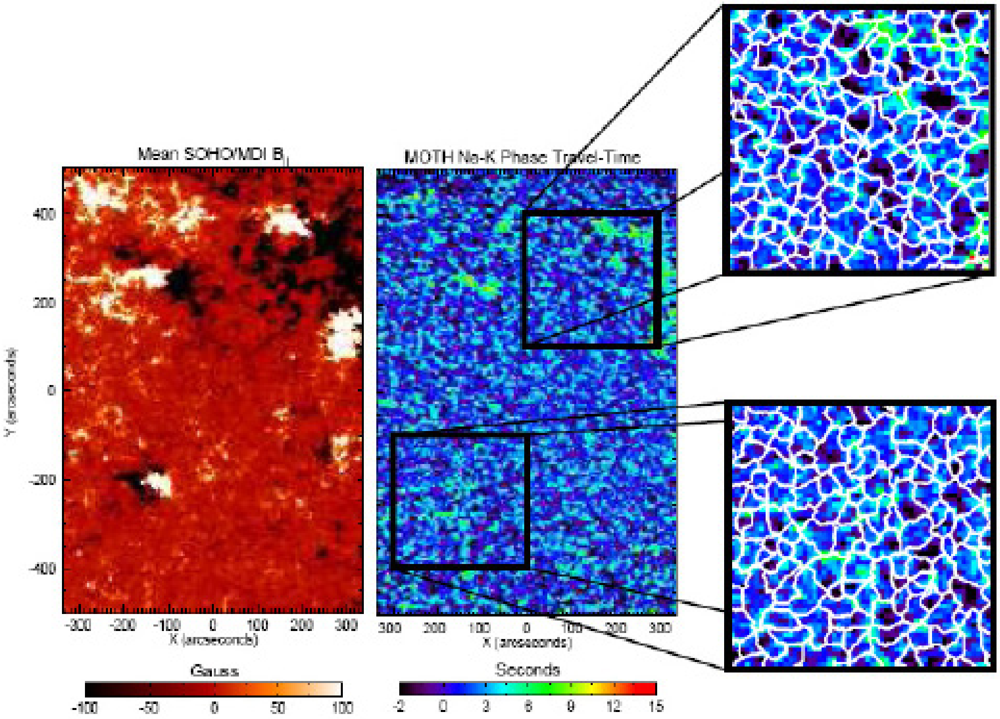

Figure 13: *(Left)* Map of the average MDI/SOHO line-of-sight component of the magnetic field in the Sun's photosphere for the 107 hr period starting 06:59 UT on 2003 January 6. *(Middle)* Map of phase travel time (Finsterle et al. 2004b) for magnetoacoustic waves with frequencies near 3 mHz based on contemporaneous, simultaneous Doppler velocity data of the full solar disk as viewed at 5890 Å (Na) and 7699 Å (K). *(Right)* Magnified views of two regions of the phase-travel-time map overlaid with an estimate of the location of the boundaries of the supergranular-scale convective cells as determined using a segmentation of the mean intensity image at 5890 Å. Note that there is not a significant travel-time signal in all of the observed plages, only in regions where the field is highly inclined. This signal is noticeably larger than that in the boundaries of the supergranules. This is probably due to the larger magnetic filling factor in the plage. Figure and caption from Jefferies et al. (2006).

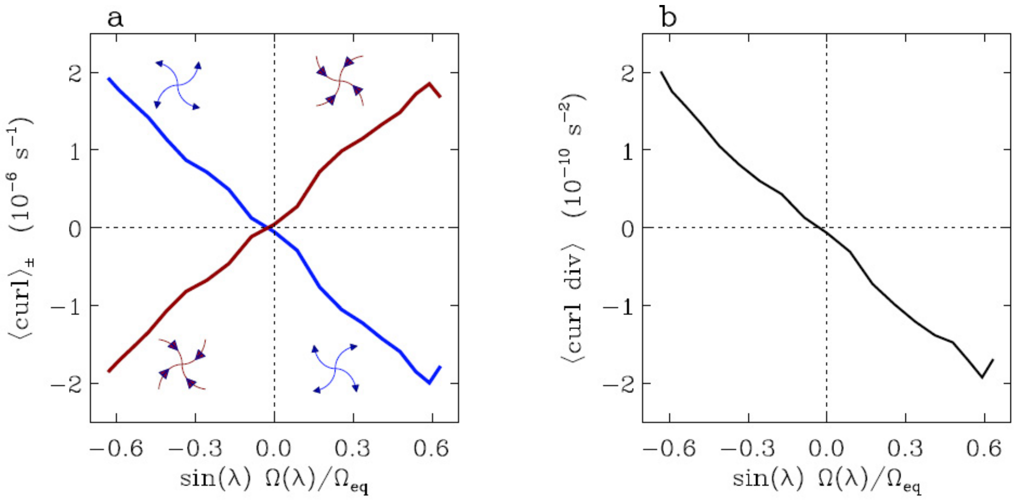

Figure 14: Effect of the Coriolis force on supergranulation flows. (*a*) Vertical vorticity (curl) averaged over regions with positive horizontal divergence ($\langle \mathrm{curl} \rangle_+$, blue curve) and negative horizontal divergence ($\langle \mathrm{curl} \rangle_-$, red curve) as functions of $\sin(\lambda)\Omega(\lambda)/\Omega_{\mathrm{eq}}$, where λ is the heliographic latitude and $\Omega/\Omega_{\mathrm{eq}}$ is the local surface angular velocity relative to the equator. A vorticity of 1 $\mathrm{M\,s^{-1}}$ corresponds to an angular velocity of 2.5° day^{-1} or a typical tangential velocity of 10 $\mathrm{m\,s^{-1}}$. (*b*) Horizontal average $\langle \mathrm{curl\ div} \rangle$ versus $\sin(\lambda)\Omega(\lambda)/\Omega_{\mathrm{eq}}$. Adapted from Gizon & Duvall (2003).

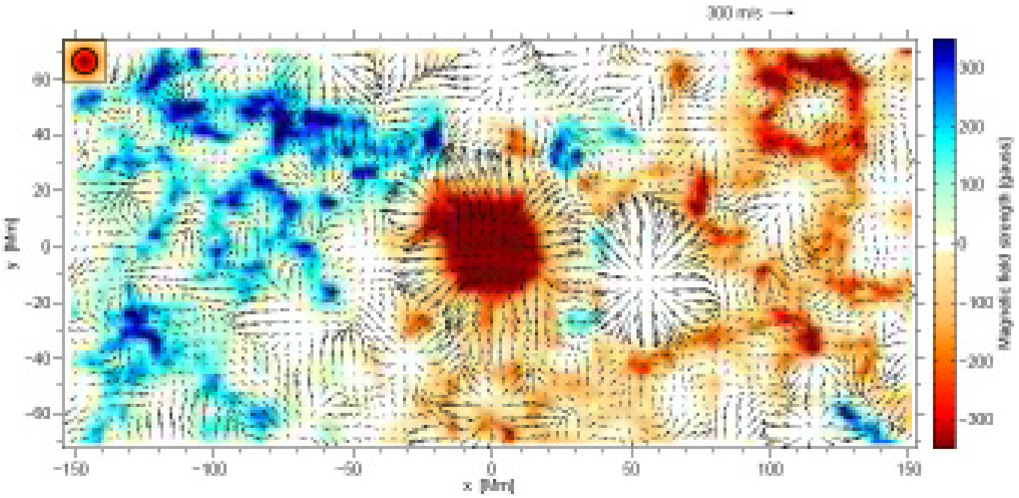

Figure 15: Moat flow around the sunspot in AR 9787 (see **Figure 2**) using the same time-distance inversion as in **Figure 12*a***. The background colors show the MDI line-of-sight component of the magnetic field. The depth is 1 Mm and the observation time is $T = 1$ day. The random noise in each horizontal component of the flow is estimated to be 17 $\mathrm{m\,s^{-1}}$. Adapted from Gizon et al. (2009) by Jason Jackiewicz.

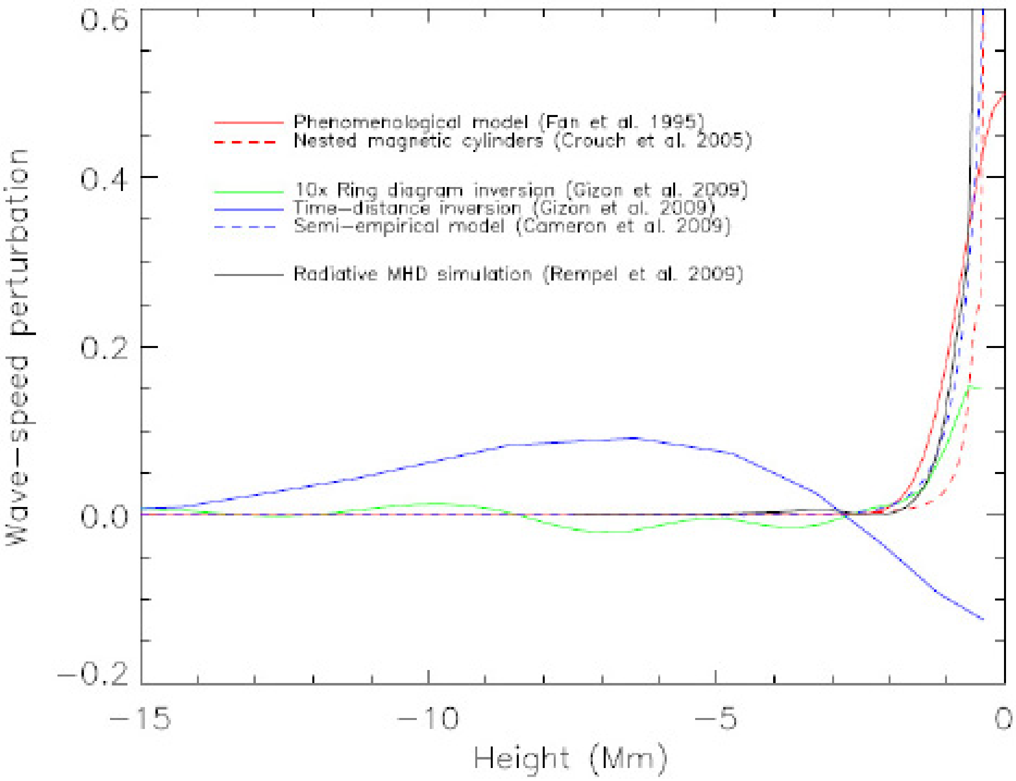

Figure 16: Wave-speed perturbations under sunspots relative to quiet Sun. The perturbations are measured along sunspot axes except for the case of (unresolved) ring-diagram analysis. The solid red line shows a phenomenological model based on the Fourier-Hankel analysis of the sunspot in active region NOAA 5254 during 27 − 30 November 1988 (Fan, Braun & Chou 1995). The dashed red curve shows the fast wave speed, $c_{\mathrm{f}} = (c^2 + a^2)^{1/2}$, in NOAA 5254 from the forward model of Crouch et al. (2005) that consists of nested magnetic cylinders. The green and solid blue lines give the wave-speed perturbations under the sunspot in active region NOAA 9787 inferred from ring-diagram analysis and time-distance helioseismology using phase-speed filters (Gizon et al. 2009). The same tracked patch (diameter 15°) was analyzed in both cases. The sunspot is not spatially resolved in the ring analysis: a factor of ten is applied to improve the comparison. This active region, which includes a long-lived sunspot and surrounding plage, was observed by SOHO/MDI during 20-27 January 2002. The two analyses give inconsistent estimates of the subsurface wave-speed perturbations averaged over the 15° patch. Possible explanations for this disagreement are described in the text. The dashed blue line is the fast wave speed of the semi-empirical model of Cameron et al. (2009, submitted), based on the umbral model of Maltby et al. (1986) and discussed in **Figure 17**. The black curve is the fast wave speed from the radiative MHD numerical simulation of Rempel et al. (2009).

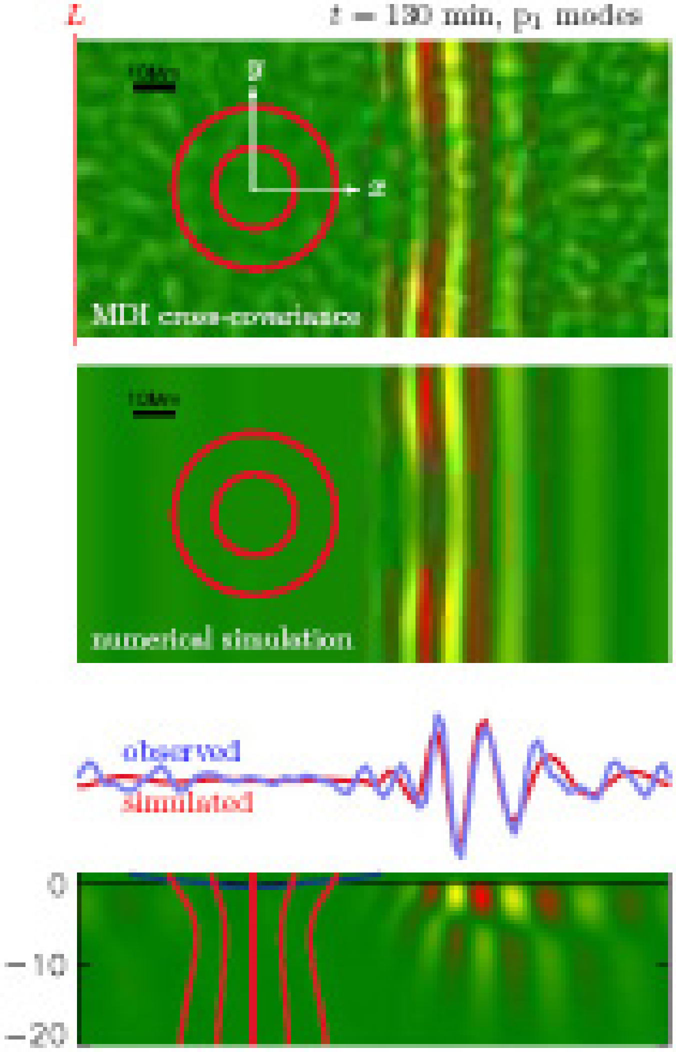

Figure 17: Sunspot time-distance helioseismology and forward numerical modeling. The top panel shows the observed covariance, $C(\mathbf{r},t) = \int dt'\overline{\phi}(t')\phi(\mathbf{r},t'+t)$, between the MDI Doppler velocity averaged over the red line (L) at $x = -40$ Mm, $\overline{\phi}(t')$, and the Doppler velocity delayed by $t = 130$ min, $\phi(\mathbf{r},t'+t)$. The horizontal coordinates $\mathbf{r} = (x,y)$ are centered on the sunspot. The color scale is such that positive values of C are red and negative values are yellow. The two red circles indicate the boundaries of the umbra and penumbra of the sunspot in Active Region 9787. The Doppler observations were filtered to select only the p_1 acoustic modes. To reduce noise, the cross-covariance was averaged over nine days (20–28 January 2002) and over angles using the azimuthal symmetry of the sunspot. The panel below shows the numerical simulation from **Figure 11**, except that the vertical component of velocity, v_z, is now shown. The initial conditions were chosen such that v_z matches the observed cross-covariance in the far field. The observed C and the simulated v_z are averaged over -2.5 Mm $< y <$ 2.5 Mm and plotted as function of x. The simulation provides a good match in phase and amplitude with the observations, for this particular model sunspot. The bottom panel shows the simulated v_z in the x–z cut through the sunspot. The vertical scale is given in units of Mm and the $a = c$ level is shown by the blue curve. See **Supplemental Movie 8**. A similar analysis was performed by Cameron, Gizon & Duvall (2008) for f-mode wave packets.

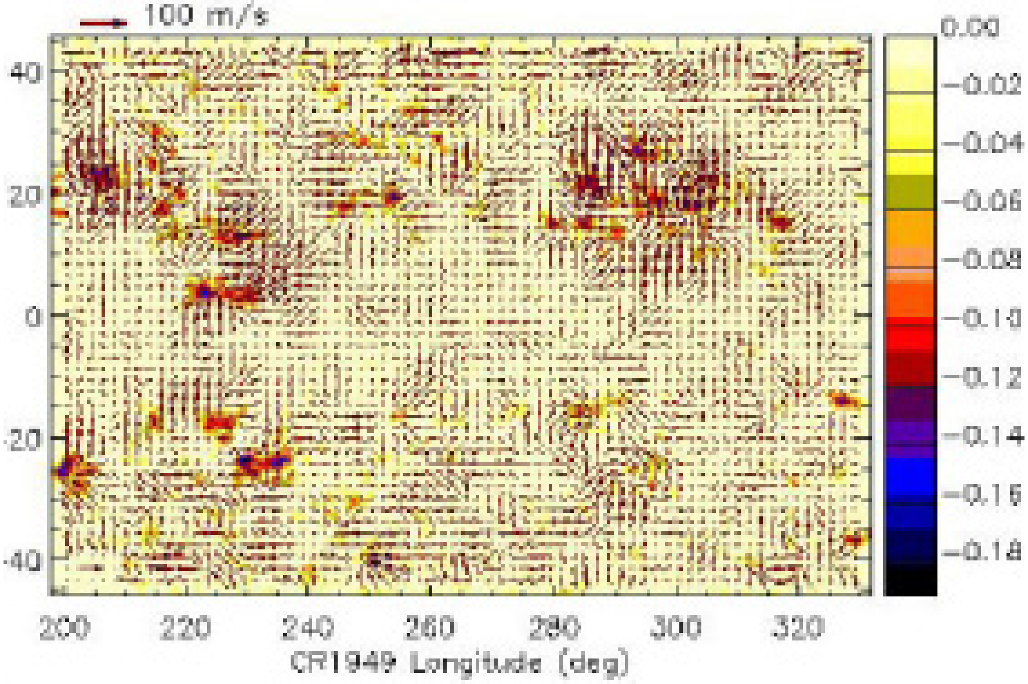

Figure 18: Synoptic map of local horizontal flows in the top 2 Mm below the solar surface, obtained with f-mode time-distance helioseismology. The horizontal and vertical axes give the longitude and the latitude in heliographic degrees. The data were averaged in time (7 days) in a frame of reference that co-rotates with the Sun (Carrington rotation rate). The flow maps were further processed to remove the average differential rotation and meridional flow. The gray scale gives the relative change in f-mode travel times: reduced travel times correlate with magnetic activity. Adapted from Gizon, Duvall & Larsen (2001).

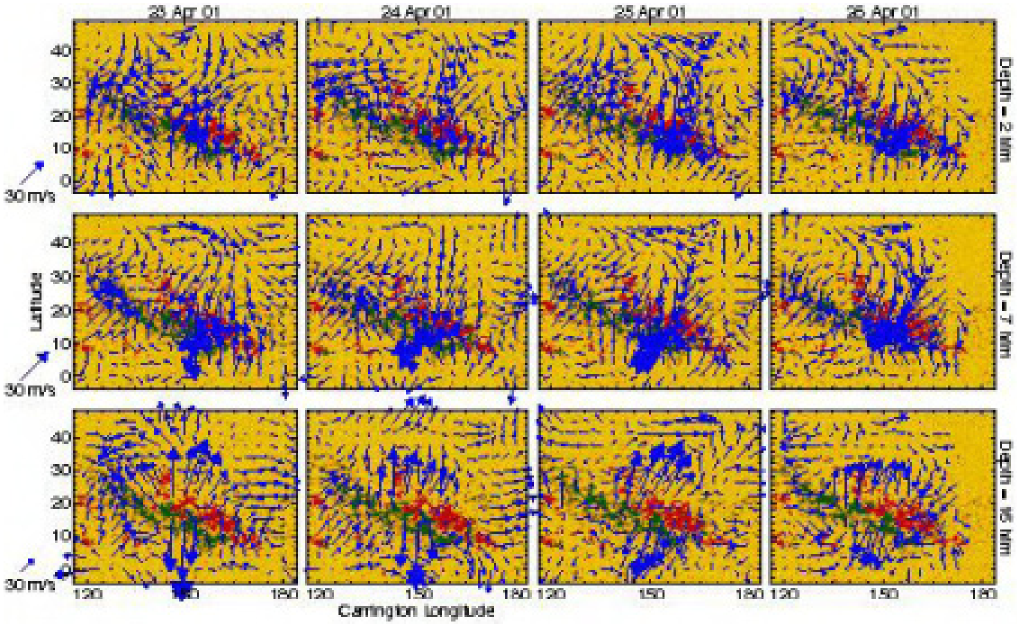

Figure 19: Daily averages of the horizontal flows around active region NOAA 9433 from 23 April until 26 April 2001 (one column for each day) inferred from ring-diagram analysis (Haber et al. 2004). The depths shown are 2 Mm (top row), 7 Mm (middle row) and 14 Mm (lower row). The green and red shades are for the two polarities of the surface magnetic field (MDI magnetograms). The transition between inflow and outflow occurs near 10 Mm depth.

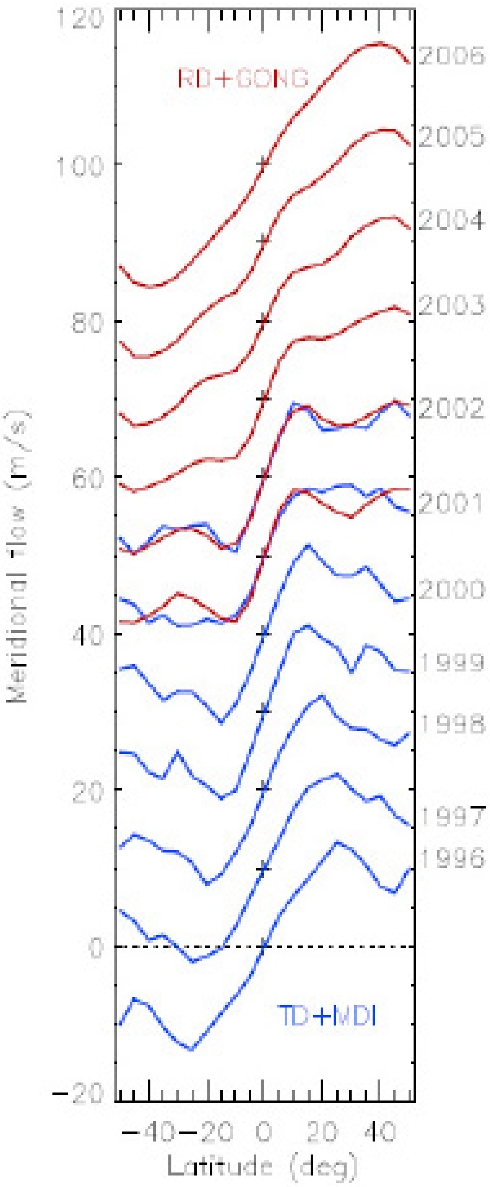

Figure 20: Anti-symmetric component of the near-surface meridional flow as a function of latitude during 1996 − 2006. Each curve corresponds to a different year as indicated on the right. To improve lisibility, years 1997 and above are shifted by multiples of 10 m s^{-1}. The blue curves until 2002 show the advection of supergranulation as measured by time-distance helioseismology (Gizon & Rempel 2008) and MDI full-disk data (2 − 3 months per year). The red curves from 2001 are averages (from the surface down to 7 Mm) of the meridional flow inferred by ring-diagram analysis and GONG data (González Hernández et al. 2008). The ring-diagram values are multiplied by a factor of 0.8 to ease the comparison. Note the local maximum moving towards the equator, from 25° in 1996 to 10° in 2006.

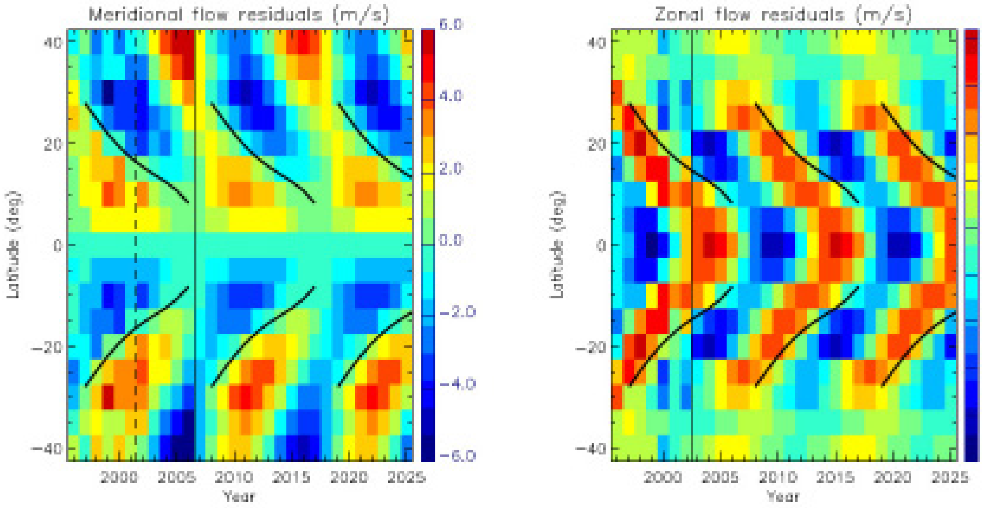

Figure 21: Solar cycle variations of the meridional and zonal flows in the near-surface layers. (*Top*) Time residuals of the meridional flow after subtraction of the average meridional flow for 1996–2006 (from **Figure 20**). The color scale is in units of $\mathrm{m\,s^{-1}}$. The first eleven years (the observations) are extrapolated into the future by fitting the eleven-year periodic component. The thick black curves represent the mean latitude of activity estimated from Mount Wilson magnetograms. (*Bottom*) Time residuals of the zonal flows after subtraction of the mean rotational velocity for the period 1996–2002, followed by the eleven-year periodic component. Flows are deduced from the advection of the supergranulation in MDI time-distance divergence maps (Gizon & Rempel 2008). The color scale is in units of $\mathrm{m\,s^{-1}}$.

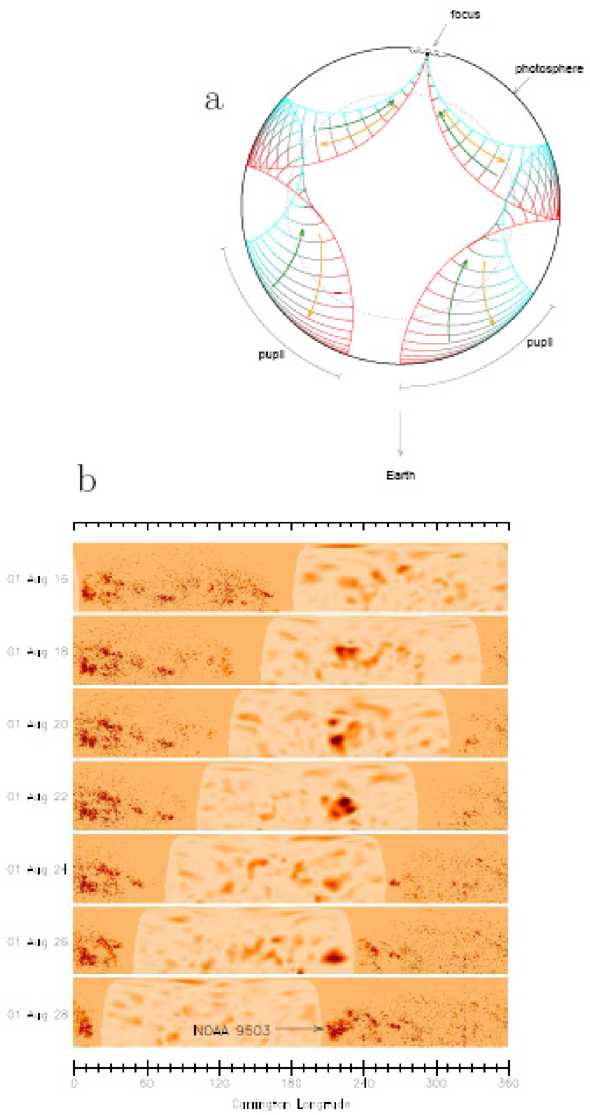

Figure 22: Farside imaging. (*a*) Ray-path diagram for 2+2 skip farside imaging (Lindsey & Braun 2000). Waves seen leaving (arriving) at the pupils on the visible surface of the Sun travel in the direction of the yellow (green) arrows. The waves skip from the solar surface once before, and once after, reaching the focal point on the farside of the Sun. Active regions located at the focal point induce small phase shifts into the waves. (*b*) GONG farside images (lighter yellow background) combined with magnetograms of the front side (darker yellow background) covering a 12 day period each. Each full-Sun map is plotted as a function of Carrington longitude (latitude in a co-rotating frame) and latitude. The active region NOAA 9503 (August 2001) is seen to form on the farside of the Sun and then rotate onto the visible disk. Courtesy of Charles Lindsey.

10 FLARE-EXCITED WAVES

The excitation of solar oscillations by a flare was first observed by Kosovichev & Zharkova (1998) using MDI data. Since then, many other examples have been found (e.g. Donea et al. 2006). **Figure 23** shows a summary of some observations of the waves generated by the flare of 15 January 2005. In this example, the location of the wave source (as estimated from helioseismic holography) is seen to nearly coincide with the hard x-ray emission as seen by the RHESSI spacecraft. The seismic waves are first seen about twenty minutes after the hard x-ray emission and propagate outwards according to the time-distance relation (**Figure 6*a***). In addition to exciting local waves, solar flares are also observed to put energy into the the very low degree global modes Karoff & Kjeldsen (2008).

The details of the physical mechanism responsible for the wave excitation are not clear. Two main suggestions have been high-energy electrons (Kosovichev 2007) and the Lorentz forces (Hudson, Fisher & Welsch 2008) due to the reconfiguration of the magnetic field during the flare. Lindsey & Donea (2008) discuss the competing mechanisms in detail. Additional observations and modeling efforts are needed in order to test these proposals.

11 FUTURE OBSERVATIONS

11.1 Solar Dynamics Observatory

The Helioseismic and Magnetic Imager (HMI) is designed to deliver ideal data for local helioseismology. HMI is one of several instruments onboard NASA's Solar Dynamics Observatory (SDO) to be flown this year in a geosynchronous orbit. HMI will transmit 4086×4096 pixel Doppler images of the Sun at the cadence of one image every 50 s or better. It will combine high spatial resolution (1 arcsec) and full spatial coverage, with a very high duty cycle over a nominal mission duration of five years. This combination will make possible the local helioseismic analysis of regions closer to the limb (less foreshortening), in order to study higher solar latitudes and the evolution of magnetic active regions as they rotate from limb to limb across the solar disk. In addition to Dopplergrams, HMI will provide images of the three components of the vector magnetic field, providing important information for the interpretation of helioseismic data. A stated goal of HMI/SDO is the subsurface detection of the magnetic field before it emerges at the surface, leading to reliable predictive capability (Kosovichev & HMI Science Team 2007). In combination with observations from the Atmospheric Imaging Assembly (AIA), a set of four SDO telescopes designed to provide an unprecedented view of the lower corona, HMI and local helioseismology will help establish relationships between the internal structure and dynamics of the Sun and the various components of magnetic activity in the solar atmosphere. SDO instruments will

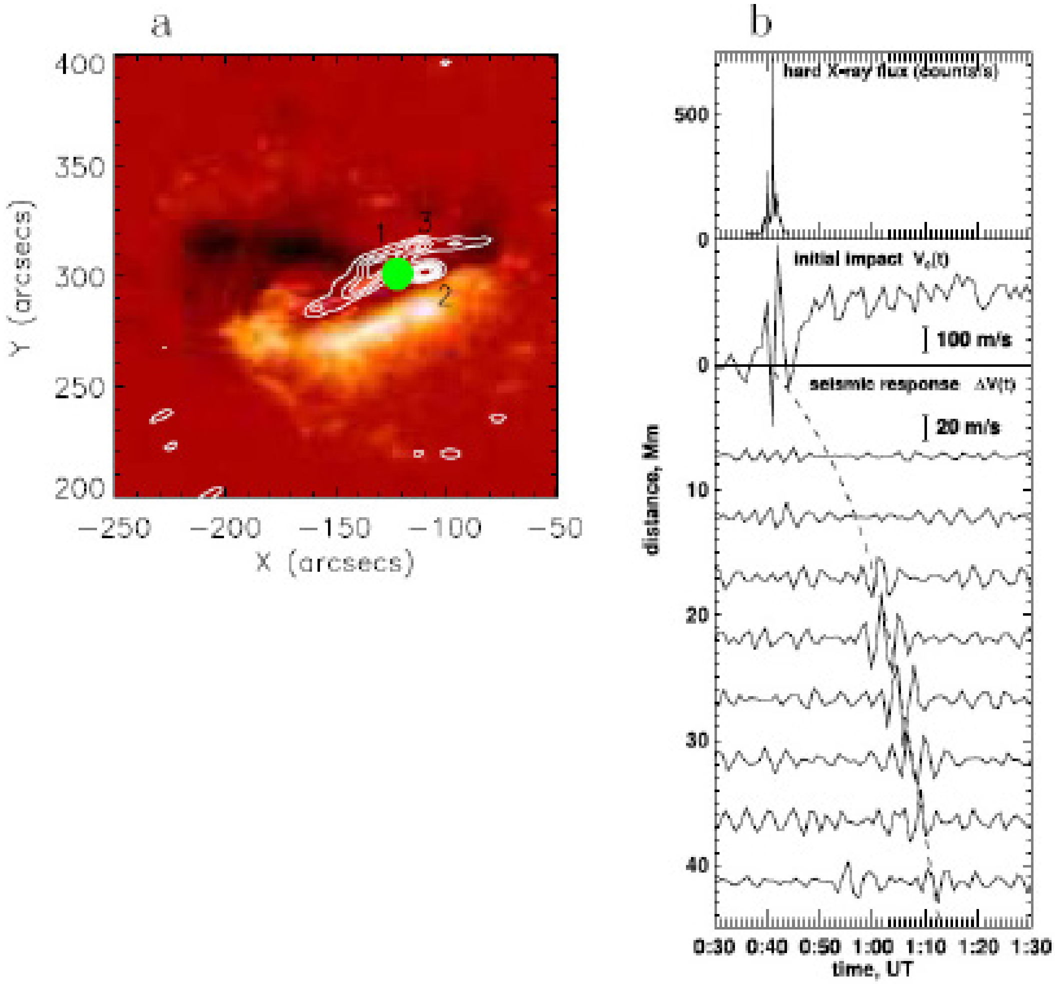

Figure 23: Flare-excited waves in Active Region NOAA 10720 on 15 January 2005. (*a*) MDI/SOHO magnetogram (color background) with RHESSI X-ray emission averaged over the period 00:41:33–00:42:34 UT (12–25 keV contours at 10, 20, 30, 40, 50, 60, and 80 per cent of the maximum flux). Three hard X-ray sources are observed. The green dot shows the location of the helioseismic source (Moradi et al. 2007). Courtesy of Alina Donea and Hamed Moradi. (*b*) Sequence of events. High-energy electrons accelerated in the solar flare interact with the lower atmosphere, producing hard X-ray emission (observed by RHESSY) and shocks leading to an initial hydrodynamic impact in the photosphere (observed by SOHO/MDI). Raw SOHO/MDI Dopplergrams reveal an expanding seismic wave about 20 min after the initial impact. The dashed curve shows a theoretical time-distance curve for helioseismic waves. Figure and caption from Kosovichev (2006). With kind permission of Springer Science and Business Media.

generate a total data flow of about 1.5 TB/day, which represents a real challenge for the ground segment in terms of data storage, processing, and analysis.

The instrumental design of HMI is similar to MDI's, except for the choice of the absorption line. Using a combined Lyot-Michelson filter system, HMI will take five filtergrams across the Fe I line at 6173 Å, separated by 69 mÅ (Borrero

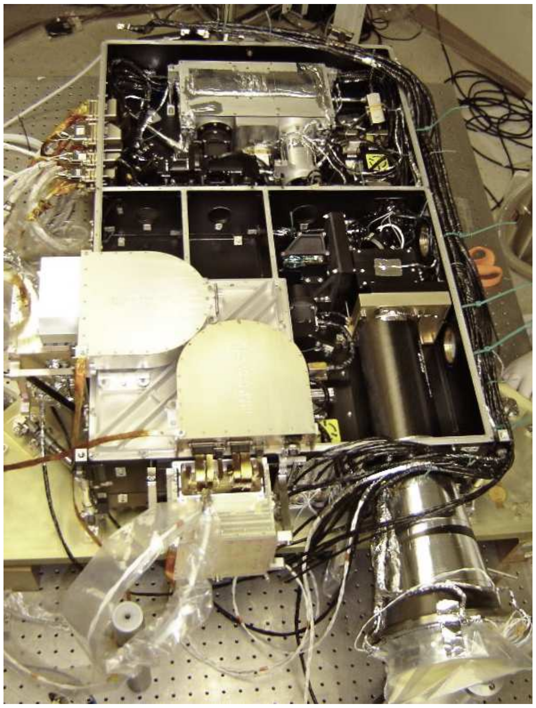

Figure 24: The HMI instrument to be flown in 2010 onboard NASA's Solar Dynamics Observatory. Courtesy of Philip Scherrer.

et al. 2007). This line has a Lande factor $g = 2.5$ and therefore is better suited for the measurement of the vector magnetic field (than e.g. the Ni 6768 line). A picture of the HMI flight model is shown in **Figure 24**. The HMI instrument was delivered in November 2007 and has been integrated onto the SDO spacecraft. At the time of writing, the launch of SDO is scheduled for February 2010 from Cape Canaveral.

11.2 Solar Orbiter

Solar Orbiter is the next solar physics mission of the European Space Agency (ESA) and a logical step after SOHO. The target launch date is 2015. Solar Orbiter will use multiple gravity assist manoeuvres at Venus and the Earth such that the inclination of the orbit to the ecliptic will incrementally increase during the course of the mission (about 10 years) to reach heliographic latitudes of at least 30°. The elliptical orbit will have a minimum perihelion distance of 0.22 AU. The scientific payload will include a remote sensing package that will deliver 0.5 arcsec pixel images of the solar photosphere (intensity, Doppler velocity, and magnetic field).

While the exact details of the orbit (and observation windows) are still being discussed, it is clear that Solar Orbiter will offer unique opportunities for helioseismology (Woch & Gizon 2007). First, it will be possible to study the subsurface flows and structure in the polar regions, which is not possible today and is important to understand the solar cycle. Second, Solar Orbiter will enable us to test and apply the concept of stereoscopic helioseismology. Stereoscopic helioseismology combines observations from different vantage points. Solar Orbiter's orbit is particularly interesting as it will offer a large range of spacecraft-Sun-Earth angles. With observations from two widely different viewing angles (Solar Orbiter and another Earth or near-Earth experiment), it becomes possible to consider acoustic ray paths with very large separation distances (see **Figure 6*b***). This is useful in local helioseismology to probe structures deep into the Sun, and, in particular, at the bottom of the convection zone.

12 SUMMARY AND OUTLOOK

Local helioseismology exploits the information contained in the local dispersion relation of the acoustic and surface-gravity waves (ring-diagram analysis) and in the correlations of the random wave field (time-distance helioseismology and related methods) in order to study the subsurface structure and dynamics of the Sun in three dimensions. The high-quality observations from the GONG network and the SOHO satellite have made possible the study of the properties of the upper layers of the convection zone and their variations with the solar cycle.

Local helioseismology has not reached maturity and there are many open questions about data analysis methods and interpretation. The observational results which, in our view, are the most robust and physically sensible are sketched in **Figure 25** and listed in the **Summary Points** below. Local helioseismology measures effects that are subtle, such as velocities of only a few $\mathrm{m\,s^{-1}}$. In addition to approximations in the data interpretation, it is important to keep in mind that several sources instrumental errors can affect the measurements, e.g., plate scale errors and optical distortion (Korzennik, Rabello-Soares & Schou 2004) or uncertainties in the orientation of the image (Giles 2000).

An important challenge for future work in local helioseismology is to detect signatures of magnetic fields at the base of the convection zone, where the field is expected to be amplified by differential rotation and stored until erupting to the surface as active regions. Direct detection through their effect on wave propagation properties is unlikely. Because of the high pressure at the base of the convection zone, the contrast in propagation speed is very much lower than in surface structures like sunspots, even at the inferred field strengths of $\sim 10^5$G. More promising is the prospect of detecting systematic flows that might be associated with magnetic structures at the base of the convection zone. Easiest to detect would be azimuthal flows (variations in rotation rate), such as have already been reported on the time scale of the solar cycle. Even if the sensitivity of helioseismic methods turns out insufficient to detect such deeply seated struc-

Figure 25:

tures, it may well be sufficient to rule out certain less-preferred classes of models for the solar cycle, such as convective dynamo models acting throughout the convection zone or in a shallow surface layer. An important class of flows would be the geostrophic flows caused by thermal effects of magnetic fields (see Section 7). Such disturbances are much easier to detect through their thermal winds than directly by their temperature contrast. They might be turned into a diagnostic of magnetic fields in deeper layers that can be probed with helioseismology.

The availability of powerful computers provides exciting opportunities to devise, validate, and optimize improved methods of local helioseismology. Exploring these possibilities will be key to taking full advantage of the observations of solar oscillations. In Sections 4.2 and 6, we have shown examples of the usefulness of numerical simulations of wave propagation through prescribed reference sunspot models. Simulations of wave propagation in spherical geometry (e.g. Hanasoge et al. 2006) have been used in time-distance studies of the deep convection zone (e.g. Zhao et al. 2009) and to validate far-side imaging (Hartlep et al. 2008).

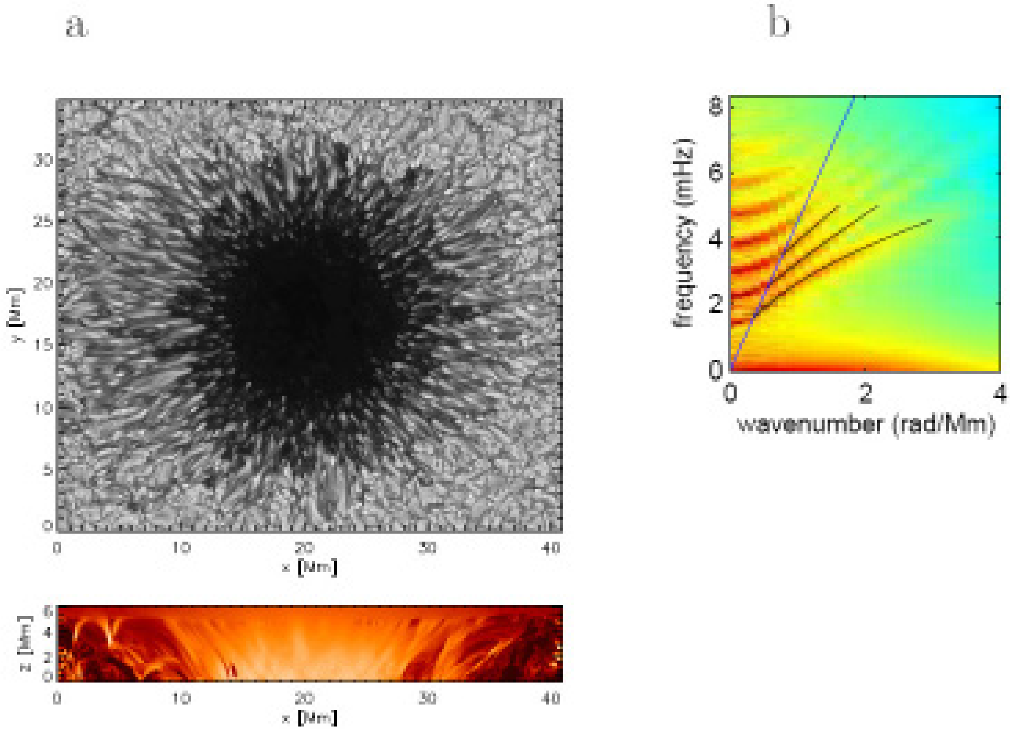

Figure 26: Radiative MHD simulation of a sunspot by Rempel et al. (2009). (*a*) Bolometric intensity (black and white) and subsurface magnetic field strength on a vertical cut through the center of the sunspot (in the range 0 − 8 kG). See **Supplemental Movie 11**. (*b*) Power spectrum of the surface oscillations in the simulation. The blue line is the phase speed at the bottom of the box, above which the model is not realistic.

It is now becoming possible to simulate the near surface layers of the Sun, including pores and sunspots, by numerically solving the radiative MHD equations (Rempel et al. 2009). **Figure 26*a*** shows a snapshot of the intensity and the magnetic field for a sunspot simulation. In this simulation, the solar oscillations are naturally excited by the convection (see **Figure 26*b***). This type of simulation provides a means for computing realistic time series of Dopplergrams, which can be used as input to all the methods of local helioseismology. With this type of data set, it will be possible to resolve some of the outstanding issues, for example regarding sunspot subsurface structure (Section 6.4). The recently achieved convergence of observations and realistic 3D radiative MHD simulations of sunspots can count as a major success story in solar physics. It adds confidence in our numerical methods and in our understanding of the physics of solar magnetic activity.

There are many complications in local helioseismology that have not been studied in detail, e.g. instrumental artifacts (point spread function, astigmatism, plate scale), interpretation of the observable (e.g., filtergrams used to construct Dopplergrams) in terms of physical conditions in the solar atmosphere, center-to-limb effects such as foreshortening, and light-of-sight projection of the solar velocity. Other complications are related to the physics of wave propagation, e.g. surface magnetic effects, scattering by time-varying heterogeneities (turbulence), multiple scattering, and physical description of wave excitation and attenuation. Understanding and, in some cases, correcting for these issues is needed to apply local helioseismology to challenging problems: deep meridional circulation (Braun & Birch 2008), detecting subsurface emerging active regions, high latitudes, statistical description of turbulent flows (e.g. Reynolds stresses), etc. In addition, inferring small amplitude perturbations in the solar interior may require may years of observations and/or appropriate spatial/temporal averaging to optimize signal-to-noise ratio.

Finally, it is worth exploring the many connections between the results of local helioseismology and global-mode helioseismology: for example, the contribution of active regions to the temporal variations of low-degree mode frequencies, comparisons of rotation measurements (e.g., 1.3-year tachocline oscillations), deep sound speed anomalies (Zhao et al. 2009), and seismic radii (González Hernández, Scherrer & Hill 2009; Kholikov & Hill 2008). In principle, local helioseismology should help provide improve surface boundary conditions for global-mode inversions.

SUMMARY POINTS

1. Local helioseismology shows that supergranules are characterized by $\sim 200\ \mathrm{m\,s^{-1}}$horizontal outflows and $\sim 20\ \mathrm{m\,s^{-1}}$upflows near the surface. Magnetic field concentrations are observed at the boundaries of supergranules and the inclined field provides portals through which low-frequency waves propagate into the chromosphere. The correlation between the horizontal divergence of the flow and the vertical component of vorticity has been measured as a function of latitude: cyclonic convection is explained by the effect of the Coriolis force. The pattern of supergranulation has (unexplained) wave-like properties.

2. The amplitudes, phases, and frequencies of the solar waves are strongly affected by sunspots. Sunspots “absorb” a fraction of the ingoing waves as they partially convert into downward propagating slow MHD waves. Sunspots are surrounded by a horizontal outflow (several hundred $\mathrm{m\,s^{-1}}$) in an annular region extending as far as twice the penumbral radius. This moat flow, which persists at least in the top 4 Mm, is consistent with direct observations of the solar surface. Little is known about the subsurface magnetic and thermal structure of sunspots. Forward modeling of the helioseismic wave field requires a surface field of several kG. Multi-height observations of solar oscillations have been used to map the sunspot magnetic canopy.

3. Local helioseismology has confirmed the latitudinal differential rotation and the increase of rotation with depth in the top ~ 35 Mm of the convection zone (near-surface shear layer). Flows in meridional planes have been measured by local helioseismology in the top ~ 50 Mm. For latitudes less than 45°, the longitudinal component of the flow is poleward, with a maximum amplitude of 15 $\mathrm{m\,s^{-1}}$. It is not clear whether the meridional flow can be detected reliably deeper or at higher latitudes.
4. The solar-cycle variation of rotation has been confirmed: bands of faster and slower rotation (± 10 $\mathrm{m\,s^{-1}}$) migrate in latitude with magnetic activity. In addition, local helioseismology has revealed that the longitudinal-average of the meridional flow also varies with the solar cycle (± 5 $\mathrm{m\,s^{-1}}$), i.e. by a significant fraction of its mean value. Near the surface, the time residuals are consistent with a North-South inflow around the mean latitude of activity. At a depth of 50 Mm, the residuals are consistent with a small outflow.
5. On intermediate scales ($\sim 20°$) weak horizontal inflows (~ 50 $\mathrm{m\,s^{-1}}$) have been detected around complexes of magnetic activity, near the surface. If confirmed, these flows may explain the time evolution of the longitudinal average of the meridional flow. At greater depths (> 10 Mm) the horizontal flows appear to switch sign and diverge from centers of magnetic activity (~ 50 $\mathrm{m\,s^{-1}}$). In addition, the surface inflows are associated with cyclonic vorticity.
6. Farside helioseismology works. Large active regions can be detected on the invisible hemisphere of the Sun, thus providing advanced warning of energetic particle events, days before they occur on the front side.

FUTURE ISSUES

1. The most pressing issue in local helioseismology is how to interpret magnetic effects, which requires new methods of analysis. This is illustrated by the fact that the standard methods of analysis yield conflicting inferences regarding sunspot structure and dynamics (see e.g. **Figure 16**). The way forward is to develop methods that incorporate appropriate physical models of the interaction of waves with strong magnetic fields near the surface. Surface magnetic effects must be accounted for before we can detect and study the magnetic field below the photosphere.
2. Instrumental artifacts often dominate realization noise and hamper the study of weak perturbations in the Sun. Ever-improving instrumentation is essential to pushing the limits of local helioseismology, especially to probe the deepest layers of the convection zone and the high-latitude meridional flow. The SDO/HMI instrument—expected to be launched in

2010—represents an important technological step towards improved observations.

3. Helioseismology has benefited from methods developed for the seismology of the Earth: normal mode theory, travel-time sensitivity kernels, interpretation of the cross-covariance, inverse methods, etc. We expect that local helioseismology will continue to learn from advances in Earth seismology: notable progress has been made on numerical simulations of wave propagation, the computation of travel time sensitivity kernels using numerical methods, and non-linear inversions of travel times (various aspects of modern seismology are discussed by, e.g., Tape et al. 2009).

ABBREVIATIONS/ACRONYMS

1. GONG: Global Oscillation Network Group
2. SOHO/MDI: Solar and Heliospheric Observatory/Michelson Doppler Imager
3. SDO/HMI: Solar Dynamics Observatory/Helioseismic and Magnetic Imager
4. HELAS: European Helio- and Asteroseismology Network
5. MHD: Magnetohydrodynamics
6. MAG waves: Magneto-Acoustic-Gravity waves
7. OLA: Optimally Localized Averaging (or Averages)
8. RLS: Regularized Least Squares

KEY TERMS/DEFINITIONS

1. Active region: Region of enhanced magnetic activity, including sunspots and diffuse magnetic field ('plage').
2. Quiet Sun: Regions with low levels of magnetic activity, away from active regions.
3. Dopplergram: Image of the line-of-sight component of velocity of the solar surface.
4. The forward problem: The problem of computing the propagation of waves through a given solar model.
5. The inverse problem: The problem of inferring solar subsurface properties from helioseismology measurements.
6. Ring-diagram analysis: Analysis of the local frequencies of solar oscillations over small patches of the solar disk.

7. Cross-covariance: Measure of similarity of two random signals as a function of a time-lag applied to one of them.
8. Time-distance diagram: cross-covariance of the helioseismic signal between two points on the surface, as a function of their separation distance and time lag.
9. Farside: Side of the Sun that is not visible from the Earth.

ANNOTATED REFERENCES

1. Bogdan (1997): Solar modes, wave packets, and rays.
2. Braun (1995): Mode absorption and mode coupling by sunspots.
3. Cameron, Gizon & Duvall (2008): Observations and modeling of the cross-covariance around a sunspot.
4. Giles et al. (1997): Inferring meridional circulation with time-distance helioseismology.
5. Gizon & Birch (2002): The forward problem and the first Born approximation.
6. Gizon & Birch (2005): Comprehensive open-access review of local helioseismology.
7. Jefferies et al. (2006): Multi-height observations of solar oscillations and magnetic portals.
8. Komm et al. (2004): Ring-diagram analysis of subsurface flows.
9. Kosovichev, Duvall & Scherrer (2000): Review of time-distance helioseismology.
10. Lindsey & Braun (2000): Imaging active regions on the farside of the Sun.

RELATED RESOURCES

1. Instrument web sites: GONG web site at `http://gong.nso.edu/` and SOHO/MDI at `http://soi.stanford.edu/`.
2. MDI Farside Graphics Viewer at `http://soi.stanford.edu/data/full_farside/farside.html`.
3. HELAS local helioseismology web site at `http://www.mps.mpg.de/projects/seismo/NA4/`. Software tools and selected data sets.
4. Solar Physics, Vol. 192, No. 1-2, pp. 1-494 (2000), Topical Issue "Helioseismic Diagnostics of Solar Convection and Activity" edited by T.L. Duvall Jr., J.W. Harvey, A.G. Kosovichev, and Z. Svestka. Table of contents available at `http://www.springerlink.com/content/h4bhbw3vdj8n/`.

5. Solar Physics, Vol. 251, No. 1-2, pp. 1-666 (2008), Topical Issue "Helioseismology, Asteroseismology, and MHD Connections" edited by L. Gizon, P. Cally, and J. Leibacher. Table of contents available at `http://www.springerlink.com/content/x548678p1725/`.

SIDE BAR: Extracting information from a random wave field

Duvall et al. (1993) first used the cross-covariance function to measure the travel time of wave packets between two locations on the solar surface. The cross-covariance averages the information over an ensemble of random waves, constructively. The concept of time-distance helioseismology has found many applications in physics, geophysics, and ocean acoustics (see reviews by Gouédard et al. 2008, Larose et al. 2006). Various experiments and observations (e.g. Shapiro et al. 2005, Weaver & Lobkis 2001) have shown that the cross-covariance is intimately connected to the Green's function, G, i.e. the response of the medium to an impulsive source. Recently, Colin de Verdière (2006) proved that in an *arbitrarily complex* medium containing an homogeneous distribution of white noise sources (variance σ^2), the cross-covariance is given by

$$\frac{\partial}{\partial t} C(\mathbf{r}_1, \mathbf{r}_2, t) = -\frac{\sigma^2}{4a} \left[G(\mathbf{r}_1, \mathbf{r}_2, t) + G(\mathbf{r}_2, \mathbf{r}_1, -t) \right], \tag{14}$$

when the integration time tends to infinity and the coefficient of attenuation (a) tends to zero. In the Fourier domain, this is equivalent to saying that C is proportional to the imaginary part of the Green's function, Im $G(\mathbf{r}_1, \mathbf{r}_2, \omega)$. Although the above assumptions are too restrictive to be applied to the solar case, it is clear that the cross-covariance is a very important diagnostics to probe media permeated by random fields (wave fields or diffuse fields).

DISCLOSURE STATEMENT

The authors are not aware of any biases that might be perceived as affecting the objectivity of this review.

ACKNOWLEDGEMENTS

LG acknowledges support from the Deutsches Zentrum für Luft- und Raumfahrt through project 'German Data Center for the Solar Dynamics Observatory,' from the European Research Council through FP-7 Starting Grant 'Seismic Imaging of the Solar Interior', and from the European Union through FP-6 Coordination Action 'European Helio- and Asteroseismology Network'. ACB acknowledges support from NASA contracts NNH06CD84C, NNH07CD25C, NNG07EI51C, and NNH09CE41C. SOHO is a mission of international collaboration between

ESA and NASA. GONG is an international collaboration sponsored by the NSF through a cooperative agreement with the Association of Universities for Research in Astronomy Inc. The MDI and HMI projects are supported by NASA under contracts to Stanford University. We are very grateful to Thomas Bogdan, Doug Braun, Paul Cally, Robert Cameron, Ashley Crouch, Alina Donea, Thomas Duvall Jr., Bernhard Fleck, Irene González Hernández, Deborah Haber, Frank Hill, Jason Jackiewicz, Rudi Komm, Alexander Kosovichev, John Leibacher, Charles Lindsey, Hamed Moradi, Matthias Rempel, Philip Scherrer, and Hannah Schunker for providing figures and/or comments.

SUPPLEMENTAL MATERIAL

11 Movies available online.

References

1. Babcock HW. 1961. *Ap. J.* 133:572
2. Baig AM, Dahlen FA, Hung SH. 2003. *Geophysical Journal International* 153:467
3. Basu S, Antia HM, Bogart RS. 2004. *Ap. J.* 610:1157
4. Basu S, Antia HM, Tripathy SC. 1999. *Ap. J.* 512:458
5. Beck JG, Gizon L, Duvall Jr. TL. 2002. *Ap. J. Lett.* 575:L47
6. Birch AC. 2008. *Journal of Physics Conference Series* 118:012009
7. Birch AC, Braun DC, Hanasoge SM, Cameron R. 2009. *Solar Phys.* 254:17
8. Birch AC, Felder G. 2004. *Ap. J.* 616:1261
9. Birch AC, Gizon L. 2007. *Astronomische Nachrichten* 328:228
10. Birch AC, Gizon L, Hindman BW, Haber DA. 2007. *Ap. J.* 662:730
11. Birch AC, Kosovichev AG. 2000. *Solar Phys.* 192:193
12. Birch AC, Kosovichev AG, Price GH, Schlottmann RB. 2001. *Ap. J. Lett.* 561:L229
13. Bogdan TJ. 1997. *Ap. J.* 477:475
14. Bogdan TJ, Cally PS. 1995. *Ap. J.* 453:919
15. Borrero JM, Tomczyk S, Norton A, Darnell T, Schou J, et al. 2007. *Solar Phys.* 240:177
16. Braun DC. 1995. *Ap. J.* 451:859
17. Braun DC, Birch AC. 2008. *Ap. J. Lett.* 689:L161
18. Braun DC, Duvall Jr. TL, Labonte BJ. 1987. *Ap. J. Lett.* 319:L27
19. Braun DC, Duvall Jr. TL, Labonte BJ. 1988. *Ap. J.* 335:1015

20. Braun DC, Duvall Jr. TL, Labonte BJ, Jefferies SM, Harvey JW, Pomerantz MA. 1992. *Ap. J. Lett.* 391:L113
21. Braun DC, Lindsey C. 2000. *Solar Phys.* 192:285
22. Braun DC, Lindsey C. 2001. *Ap. J. Lett.* 560:L189
23. Braun DC, Lindsey C. 2003. In *GONG+ 2002. Local and Global Helioseismology: the Present and Future*, ed. H Sawaya-Lacoste, vol. 517 of *ESA Special Publication*
24. Brickhouse NS, Labonte BJ. 1988. *Solar Phys.* 115:43
25. Busse FH. 2007. *Solar Phys.* 245:27
26. Cabrera Solana D, Bellot Rubio LR, Beck C, del Toro Iniesta JC. 2006. *Ap. J. Lett.* 649:L41
27. Cally PS. 2000. *Solar Phys.* 192:395
28. Cally PS. 2007. *Astronomische Nachrichten* 328:286
29. Cally PS, Bogdan TJ. 1993. *Ap. J.* 402:721
30. Cally PS, Bogdan TJ. 1997. *Ap. J. Lett.* 486:L67
31. Cally PS, Crouch AD, Braun DC. 2003. *MNRAS* 346:381
32. Cally PS, Goossens M. 2008. *Solar Phys.* 251:251
33. Cameron R, Gizon L, Daiffallah K. 2007. *Astronomische Nachrichten* 328:313
34. Cameron R, Gizon L, Duvall Jr. TL. 2008. *Solar Phys.* 251:291
35. Chang HK, Chou DY, Labonte BJ, The TON Team. 1997. *Nature* 389:825
36. Charbonneau P. 2005. *Living Reviews in Solar Physics* 2:2
37. Cheung MCM, Schüssler M, Tarbell TD, Title AM. 2008. *Ap. J.* 687:1373
38. Chou DY, Dai DC. 2001. *Ap. J. Lett.* 559:L175
39. Chou DY, Sun MT, Huang TY, Lai SP, Chi PJ, et al. 1995. *Solar Phys.* 160:237
40. Christensen-Dalsgaard J. 2002. *Reviews of Modern Physics* 74:1073
41. Christensen-Dalsgaard J, Dappen W, Ajukov SV, Anderson ER, Antia HM, et al. 1996. *Science* 272:1286
42. Christensen-Dalsgaard J, Schou J, Thompson MJ. 1990. *MNRAS* 242:353
43. Colin de Verdière Y. 2006. *Mathematical Models for Passive Imaging. I. General Background.* `http://arxiv.org/abs/math-ph/0610043v1`
44. Couvidat S, Birch AC, Kosovichev AG. 2006. *Ap. J.* 640:516
45. Couvidat S, Gizon L, Birch AC, Larsen RM, Kosovichev AG. 2005. *Ap. J. Suppl.* 158:217
46. Covas E, Tavakol R, Moss D, Tworkowski A. 2000. *Astron. Astrophys.* 360:L21

47. Cowling TG. 1953. Solar Electrodynamics. In *The Solar System.* Vol. 1: *The Sun*, ed. GP Kuiper, 8:532. Chicago: The University of Chicago Press
48. Crouch AD, Cally PS. 2005. *Solar Phys.* 227:1
49. Crouch AD, Cally PS, Charbonneau P, Braun DC, Desjardins M. 2005. *MNRAS* 363:1188
50. Dahlen FA, Hung SH, Nolet G. 2000. *Geophysical Journal International* 141:157
51. De Rosa M, Duvall Jr. TL, Toomre J. 2000. *Solar Phys.* 192:351
52. Dikpati M, Charbonneau P. 1999. *Ap. J.* 518:508
53. Donea AC, Besliu-Ionescu D, Cally P, Lindsey C. 2006. In *Solar MHD Theory and Observations: A High Spatial Resolution Perspective*, eds. J Leibacher, RF Stein, H Uitenbroek, vol. 354 of *Astronomical Society of the Pacific Conference Series*
54. Duvall TL, D'Silva S, Jefferies SM, Harvey JW, Schou J. 1996. *Nature* 379:235
55. Duvall Jr. TL. 1998. In *Structure and Dynamics of the Interior of the Sun and Sun-like Stars*, ed. S Korzennik, vol. 418 of *ESA Special Publication*
56. Duvall Jr. TL, Birch AC, Gizon L. 2006. *Ap. J.* 646:553
57. Duvall Jr. TL, Gizon L. 2000. *Solar Phys.* 192:177
58. Duvall Jr. TL, Jefferies SM, Harvey JW, Pomerantz MA. 1993. *Nature* 362:430
59. Duvall Jr. TL, Kosovichev AG, Scherrer PH, Bogart RS, Bush RI, et al. 1997. *Solar Phys.* 170:63
60. Fan Y, Braun DC, Chou DY. 1995. *Ap. J.* 451:877
61. Finsterle W, Jefferies SM, Cacciani A, Rapex P, Giebink C, et al. 2004a. *Solar Phys.* 220:317
62. Finsterle W, Jefferies SM, Cacciani A, Rapex P, McIntosh SW. 2004b. *Ap. J. Lett.* 613:L185
63. Galloway DJ, Proctor MRE, Weiss NO. 1977. *Nature* 266:686
64. Giles PM. 2000. *Time-distance measurements of large-scale flows in the solar convection zone.* Ph.D. thesis, Stanford Univ.
65. Giles PM, Duvall Jr. TL, Scherrer PH. 1998. In *Structure and Dynamics of the Interior of the Sun and Sun-like Stars*, ed. S Korzennik, vol. 418 of *ESA Special Publication*
66. Giles PM, Duvall Jr. TL, Scherrer PH, Bogart RS. 1997. *Nature* 390:52
67. Gizon L. 2003. *Probing flows in the upper solar convection zone.* Ph.D. thesis, Stanford Univ.
68. Gizon L, Birch AC. 2002. *Ap. J.* 571:966
69. Gizon L, Birch AC. 2004. *Ap. J.* 614:472

70. Gizon L, Birch AC. 2005. *Living Reviews in Solar Physics* 2:6

71. Gizon L, Duvall TL. 2003. In *GONG+ 2002. Local and Global Helioseismology: the Present and Future*, ed. H Sawaya-Lacoste, vol. 517 of *ESA Special Publication*

72. Gizon L, Duvall TL, Schou J. 2003. *Nature* 421:43

73. Gizon L, Duvall Jr. TL, Larsen RM. 2000. *Journal of Astrophysics and Astronomy* 21:339

74. Gizon L, Duvall Jr. TL, Larsen RM. 2001. In *Recent Insights into the Physics of the Sun and Heliosphere: Highlights from SOHO and Other Space Missions*, eds. P Brekke, B Fleck, JB Gurman, vol. 203 of *IAU Symposium*

75. Gizon L, Hanasoge SM, Birch AC. 2006. *Ap. J.* 643:549

76. Gizon L, Rempel M. 2008. *Solar Phys.* 251:241

77. Gizon L, Schunker H, Baldner CS, Basu S, Birch AC, et al. 2009. *Space Science Reviews* 144:249

78. Gizon L, Thompson MJ. 2007. *Astronomische Nachrichten* 328:204

79. González Hernández I, Hill F, Lindsey C. 2007. *Ap. J.* 669:1382

80. González Hernández I, Kholikov S, Hill F, Howe R, Komm R. 2008. *Solar Phys.* 252:235

81. González Hernández I, Komm R, Hill F, Howe R, Corbard T, Haber DA. 2006. *Ap. J.* 638:576

82. González Hernández I, Scherrer P, Hill F. 2009. *Ap. J. Lett.* 691:L87

83. Gouédard P, Stehly L, Brenguier F, Campillo M, Colin de Verdière Y, et al. 2008. *Geophysical Prospecting* 56:375

84. Haber DA, Hindman BW, Toomre J, Bogart RS, Hill F. 2001. In *SOHO 10/GONG 2000 Workshop: Helio- and Asteroseismology at the Dawn of the Millennium*, eds. A Wilson, PL Pallé, vol. 464 of *ESA Special Publication*

85. Haber DA, Hindman BW, Toomre J, Bogart RS, Thompson MJ, Hill F. 2000. *Solar Phys.* 192:335

86. Haber DA, Hindman BW, Toomre J, Thompson MJ. 2004. *Solar Phys.* 220:371

87. Hanasoge SM. 2008. *Ap. J.* 680:1457

88. Hanasoge SM, Larsen RM, Duvall Jr. TL, DeRosa ML, Hurlburt NE, et al. 2006. *Ap. J.* 648:1268

89. Hartlep T, Zhao J, Mansour NN, Kosovichev AG. 2008. *Ap. J.* 689:1373

90. Harvey J, The GONG Instrument Team. 1995. In *GONG 1994. Helio- and Astro-Seismology from the Earth and Space*, eds. RK Ulrich, EJ Rhodes Jr., W Dappen, vol. 76 of *Astronomical Society of the Pacific Conference Series*

91. Harvey JW, Hill F, Hubbard R, Kennedy JR, Leibacher JW, et al. 1996. *Science* 272:1284
92. Hathaway DH. 1996. *Ap. J.* 460:1027
93. Hathaway DH, Beck JG, Han S, Raymond J. 2002. *Solar Phys.* 205:25–38
94. Hathaway DH, Nandy D, Wilson RM, Reichmann EJ. 2003. *Ap. J.* 589:665
95. Hathaway DH, Williams PE, Cuntz M. 2006. *Ap. J.* 644:598
96. Heinemann T, Nordlund Å, Scharmer GB, Spruit HC. 2007. *Ap. J.* 669:1390
97. Hill F. 1988. *Ap. J.* 333:996
98. Hill F. 1989. *Ap. J. Lett.* 343:L69
99. Hindman BW, Gizon L, Duvall Jr. TL, Haber DA, Toomre J. 2004. *Ap. J.* 613:1253
100. Howard R, Labonte BJ. 1980. *Ap. J. Lett.* 239:L33
101. Howe R, Christensen-Dalsgaard J, Hill F, Komm R, Schou J, Thompson MJ. 2005. *Ap. J.* 634:1405
102. Hudson HS, Fisher GH, Welsch BT. 2008. In *Subsurface and Atmospheric Influences on Solar Activity*, eds. R Howe, RW Komm, KS Balasubramaniam, GJD Petrie, vol. 383 of *Astronomical Society of the Pacific Conference Series*
103. Hung SH, Dahlen FA, Nolet G. 2000. *Geophysical Journal International* 141:175
104. Hung SH, Dahlen FA, Nolet G. 2001. *Geophysical Journal International* 146:289
105. Jackiewicz J, Gizon L, Birch AC. 2008. *Solar Phys.* 251:381
106. Jackiewicz J, Gizon L, Birch AC, Duvall Jr. TL. 2007. *Ap. J.* 671:1051
107. Jacobsen BH, Moller I, Jensen JM, Efferso F. 1999. *Phys. Chem. Earth* 24:215
108. Jefferies SM, McIntosh SW, Armstrong JD, Bogdan TJ, Cacciani A, Fleck B. 2006. *Ap. J. Lett.* 648:L151
109. Jensen JM, Duvall Jr. TL, Jacobsen BH, Christensen-Dalsgaard J. 2001. *Ap. J. Lett.* 553:L193
110. Jensen JM, Jacobsen BH, Christensen-Dalsgaard J. 2000. *Solar Phys.* 192:231
111. Karoff C, Kjeldsen H. 2008. *Ap. J. Lett.* 678:L73
112. Kholikov S, Hill F. 2008. *Solar Phys.* 251:157
113. Khomenko E, Collados M. 2006. *Ap. J.* 653:739
114. Kitchatinov LL, Pipin VV, Makarov VI, Tlatov AG. 1999. *Solar Phys.* 189:227
115. Komm R, Corbard T, Durney BR, González Hernández I, Hill F, et al. 2004. *Ap. J.* 605:554
116. Komm R, Howe R, Hill F. 2006. *Advances in Space Research* 38:845
117. Komm R, Howe R, Hill F, Miesch M, Haber D, Hindman B. 2007. *Ap. J.* 667:571

118. Komm RW, Howard RF, Harvey JW. 1993a. *Solar Phys.* 147:207

119. Komm RW, Howard RF, Harvey JW. 1993b. *Solar Phys.* 145:1

120. Korzennik SG, Rabello-Soares MC, Schou J. 2004. *Ap. J.* 602:481

121. Kosovichev AG. 1996. *Ap. J. Lett.* 461:L55

122. Kosovichev AG. 2006. *Solar Phys.* 238:1

123. Kosovichev AG. 2007. *Ap. J. Lett.* 670:L65

124. Kosovichev AG. 2008. *Advances in Space Research* 41:830

125. Kosovichev AG, Duvall TL, Birch AC, Gizon L, Scherrer PH, Zhao J. 2002. *Advances in Space Research* 29:1899

126. Kosovichev AG, Duvall TLJ, Scherrer PH. 2000. *Solar Phys.* 192:159

127. Kosovichev AG, Duvall Jr. TL. 1997. In *SCORe'96 : Solar Convection and Oscillations and their Relationship*, eds. FP Pijpers, J Christensen-Dalsgaard, CS Rosenthal, vol. 225 of *Astrophysics and Space Science Library*

128. Kosovichev AG, HMI Science Team. 2007. *Astronomische Nachrichten* 328:339

129. Kosovichev AG, Zharkova VV. 1998. *Nature* 393:317

130. Küker M, Rüdiger G, Pipin VV. 1996. *Astron. Astrophys.* 312:615

131. Larose E, Margerin L, Derode A, van Tiggelen B, Campillo M, et al. 2006. *Geophysics* 71:11

132. Leibacher JW, Stein RF. 1971. Astrophys. Lett. 7:191

133. Leighton RB. 1969. *Ap. J.* 156:1

134. Leighton RB, Noyes RW, Simon GW. 1962. *Ap. J.* 135:474

135. Lindsey C, Braun DC. 1997. *Ap. J.* 485:895

136. Lindsey C, Braun DC. 2000. *Science* 287:1799

137. Lindsey C, Braun DC, Jefferies SM, Woodard MF, Fan Y, et al. 1996. *Ap. J.* 470:636

138. Lindsey C, Donea A. 2008. *Solar Phys.* 251:627

139. Maltby P, Avrett EH, Carlsson M, Kjeldseth-Moe O, Kurucz RL, Loeser R. 1986. *Ap. J.* 306:284

140. Marquering H, Dahlen FA, Nolet G. 1999. *Geophysical Journal International* 137:805

141. Miesch MS. 2005. *Living Reviews in Solar Physics* 2:1

142. Miesch MS, Brun AS, Toomre J. 2006. *Ap. J.* 641:618

143. Mitra-Kraev U, Kosovichev AG, Sekii T. 2008. *Astron. Astrophys.* 481:L1

144. Montelli R, Nolet G, Dahlen FA, Masters G, Engdahl ER, Hung SH. 2004. *Science* 303:338

145. Moradi H, Donea AC, Lindsey C, Besliu-Ionescu D, Cally PS. 2007. *MNRAS* 374:1155

146. Nye A, Bruning D, Labonte BJ. 1988. *Solar Phys.* 115:251

147. Parchevsky KV, Kosovichev AG. 2009. *Ap. J.* 694:573

148. Parker EN. 1979. *Cosmical magnetic fields: Their origin and their activity.* New York: Oxford University Press. 860 pp.

149. Petrovay K, Forgács-dajka E. 2002. *Solar Phys.* 205:39

150. Rempel M. 2005. *Ap. J.* 622:1320

151. Rempel M. 2007. *Ap. J.* 655:651

152. Rempel M. 2008. *Journal of Physics Conference Series* 118:012032

153. Rempel M, Schüssler M, Cameron RH, Knölker M. 2009. *Science* 325:171

154. Scherrer PH, Bogart RS, Bush RI, Hoeksema JT, Kosovichev AG, et al. 1995. *Solar Phys.* 162:129–188

155. Schlüter A, Temesváry S. 1958. In *Electromagnetic Phenomena in Cosmical Physics*, ed. B Lehnert, vol. 6 of *IAU Symposium*

156. Schou J, Antia HM, Basu S, Bogart RS, Bush RI, et al. 1998. *Ap. J.* 505:390

157. Schou J, Bogart R. 1998. *Astrophys. J. Lett.* 504:L131

158. Schunker H, Cally PS. 2006. *MNRAS* 372:551

159. Schüssler M. 1981. *Astron. Astrophys.* 94:L17

160. Schüssler M, Caligari P, Ferriz-Mas A, Moreno-Insertis F. 1994. *Astron. Astrophys.* 281:L69

161. Schüssler M, Schmitt D. 2004. *Astron. Astrophys.* 421:349

162. Shapiro NM, Campillo M, Stehly L, Ritzwoller MH. 2005. *Science* 307:1615

163. Sheeley Jr. NR. 1972. *Solar Phys.* 25:98

164. Solanki SK. 2003. *Astron. Astrophys. Rev.* 11:153

165. Spruit H. 1997. *Memorie della Societa Astronomica Italiana* 68:397

166. Spruit HC. 2003. *Solar Phys.* 213:1

167. Spruit HC, Bogdan TJ. 1992. *Ap. J. Lett.* 391:L109

168. Tape C, Liu Q, Maggi A, Tromp J. 2009. *Science* 325:988

169. Thompson MJ, Christensen-Dalsgaard J, Miesch MS, Toomre J. 2003. ARA&A 41:599

170. Thompson MJ, Zharkov S. 2008. *Solar Phys.* 251:225

171. Ulrich RK. 1970. *Ap. J.* 162:993

172. Ulrich RK, Boyden JE, Webster L, Padilla SP, Snodgrass HB. 1988. *Solar Phys.* 117:291

173. Švanda M, Zhao J, Kosovichev AG. 2007. *Solar Phys.* 241:27
174. Vorontsov SV, Christensen-Dalsgaard J, Schou J, Strakhov VN, Thompson MJ. 2002. *Science* 296:101
175. Weaver RL, Lobkis OI. 2001. *Phys. Rev. Lett.* 87:134301
176. Woch J, Gizon L. 2007. *Astronomische Nachrichten* 328:362
177. Woodard M. 2009. *Ap. J., accepted*
178. Woodard MF. 2002. *Ap. J.* 565:634
179. Woodard MF. 2007. *Ap. J.* 668:1189
180. Yoshimura H. 1981. *Ap. J.* 247:1102
181. Zhao J. 2007. *Ap. J. Lett.* 664:L139
182. Zhao J, Hartlep T, Kosovichev AG, Mansour NN. 2009. *Ap. J.* 702:1150
183. Zhao J, Kosovichev AG. 2003. In *GONG+ 2002. Local and Global Helioseismology: the Present and Future*, ed. H Sawaya-Lacoste, vol. 517 of *ESA Special Publication*
184. Zhao J, Kosovichev AG. 2004. *Ap. J.* 603:776